Wiener-Hopf Analysis of Planar Canonical Structures Loaded with Longitudinally Magnetized Plasma Biased Normally to the Extraordinary Wave Propagation: Near and Far Field

Xenofon M. Mitsalas[1], Theodoros N. Kaifas[2], and George A. Kyriacou[1, *]

Abstract—This work aims at completing the Wiener-Hopf analysis of a canonical problem referring to an extra-ordinary transverse electromagnetic wave propagating within a parallel plane waveguide loaded with magnetized plasma when incident normally at the truncated edge of its upper conductor. The complicated mathematical issues faced herein comes from the non-symmetric Kernel functions involved in the related integral equation. This property puts two challenging issues, first the rarely occurring factorization of non-symmetric Kernels and secondly the handling of unidirectional surface and leaky waves. Although the formulation of the Wiener-Hopf equations was carried out in our previous work, these two challenges were not confronted, since that work has been completed only in regard to the closed-shielded geometry which involves a symmetric Kernel. Thus, the novel contribution of this work refers to completing the analysis of the open geometry by handling the factorization of the related non-symmetric Kernel, evaluating the radiated field as well as studying the unidirectional waves for their near and far fields.

1. INTRODUCTION

Magnetized ferrites and plasmas offer unique non-reciprocal features as well as tunability by means of an electric control of their constitutive parameters. Ferrites have been exploited in the past, initially for waveguide and later for printed structures of various forms, including thick and thin films. Although the properties of ionized gas plasma were known long ago, its exploitation in microwave devices was only stimulated when the cryogenic solid state plasma technology became available, e.g., Hoyaux and Gans [1], Bolle and Chabries [2, 3]. Oliner and Tamir [4–6] gave a comprehensive treatment of the electromagnetic field of a source-excited, isotropic plasma slab. When ferrite or plasma materials are subject to constant magnetic field, they exhibit anisotropic permeability $\overline{\overline{\mu}}_r$ and permittivity $\overline{\overline{\epsilon}}_r$, respectively. These tensors' entries depend on both the biasing magnetic field and the operating frequency. This dependence enables their dynamic control through the dc current of an electromagnet which generates the biasing constant magnetic field H_{DC}. These features offered by ferrites are extensively used in microwave waveguides, stripline, and microstrip devices. A significant additional feature offered by magnetized plasma is the expanded range of relative permittivity compared to the smaller range of relative permeability in magnetized ferrites. Also, the roles of perfect electric and perfect magnetic walls are interchanged in plasma and ferrite applications, following a TEM duality principle.

In the case of an isotropic plasma substrate, the structure under consideration is widely used as a radiating device. The corresponding isotropic problem was investigated first by Angulo and Chang [7],

* Corresponding author: George A. Kyriacou (gkyriac@ee.duth.gr).
[1] Microwaves Lab, Department of Electrical and Computer Engineering, Democritus University of Thrace, Xanthi, Greece. [2] Department of Physics, Aristotle University of Thessaloniki, Greece.

in the case of the dominant TEM polarization of the exciting field and later by Bates and Mittra [8], who were concerned with both TE_{10} and TEM excitation. Compared with the isotropic case and leaving aside the obviously existing geometrical and physical similarities, the anisotropic substrate problem treated herein exhibits several unique features. Our previous effort [9], directed towards the solution of a canonical problem of a TEM wave propagating in a parallel-plane waveguide with a semi-infinite upper conductor loaded with a magnetized plasma and normally incident on the edge defined by the truncated upper conductor, as depicted in Fig. 1. The Wiener-Hopf equations are already formulated in [9], but the Kernel factorization for the estimation of the scattered field at the edge and consequently the reflected TEM wave propagating back in the parallel plane region was carried out only for the closed shielded geometry shown in Fig. 1(a). The shielded geometry results from the placement of a metallic shield parallel to the waveguide planes. As far as the open radiating structure is concerned, the analysis was restricted only on the formulation of the Wiener-Hopf equations.

The present effort aims at the factorization of the Wiener-Hopf equation for the open geometry problem shown in Fig. 1(b) in order to estimate the scattered and reflected field. Unique features regarding the discrete propagating modes and the continuous spectrum contribution to the radiated field are extensively analyzed herein. Explicitly, interesting phenomena regarding the excitation of surface and leaky waves in the grounded plasma region and the radiating space wave are involved in the scattered field expressions. The dependence of the modes turn on/off conditions of the plasma parameters and especially the magnetizing dc field are of particular importance. Reviewing the relative subject, we must note that wave phenomena on grounded plasma slabs have been studied by Seshadri and Pickard [10]. Also, towards the direction of solving scattering problems of TM waves on truncated parallel plane waveguides using Wiener-Hopf, the work of Pathak and Kouyoumjian [11] is of primary importance. An insight in the radiation characteristics of surface waves in a parallel plane waveguide, which is embedded not in free space but in homogeneous anisotropic plasma, is also provided by Johansen [12]. Higher order modes of this grounded structure are expected to become leaky waves. These waves offer non-reciprocal features in their radiation mechanisms. All these types of modes are indeed involved in the mathematical formulation and are required for the scattered and radiated field evaluation. Special attention is devoted to the study of unidirectional leaky waves that concentrate their energy either on the upper or the bottom surface of the slab. Working toward this direction, some preliminary results on the study of modes supported by the grounded magnetized plasma are published in [13]. As a consequence of the anisotropy, the derived Wiener-Hopf equation is characterized by a non-symmetric Kernel function. This is in contrast to all isotropic problems treated by the same method which are characterized by even Kernel functions, for which suitable decomposition techniques have been developed in the past, e.g., Mittra and Lee [14, p. 91, 114], Bates and Mittra [15]. Herein, the lack of symmetry affects the factorization procedure. This is clearly exhibited in the form of the resulting two factors from which only one is characterized by even symmetry. The factorization methodology of non-symmetric Kernels, as proposed by Fikioris et al. [16], is adopted herein. Explicitly in [16] the non-symmetric Kernel is factorized through a modification of a classical technique for even Kernels proposed by Mittra, Bates, and Lee [8, 14, 15].

As explained in our previous work [2] as well as in numerous publications on similar canonical problems (e.g., Kuester et al. [34], El-Sheribny [35]), the resulting analytical formulas can be exploited in various printed structures. Important contributions towards this direction consist of the work of Talisa and Bolle [37], where a GaAs semiconductor is treated at cryogenic temperature, emulating solid state plasma, in order to utilize non-reciprocal devices in the millimeter wave range. The quite optimistic view in solid state plasma applications continues at lower frequency ranges, especially in the zone of 4.5–40 GHz [38]. As stated by Iqbal and Gibson in [38], semiconducting solid-state plasma may be preferable in phase shifters than ferrites, since their losses become more manageable. Explicitly, based on the established reflection coefficient an accurate analysis of a tunable microstrip line printed on a magnetized plasma can be studied as in [36]. The microstrip line is composed of two parallel edges — apertures on which the scattering phenomena are governed by the present analysis. Important microwave structures such as tunable filters, tunable phase shifters, true-time delay lines, circulators, and isolators can be built using this type of microstrip lines [37, 38]. Its important features exploited in these applications are the electrical tunability of the magnetized solid-state plasma as well as the controllable non-reciprocal phenomena. From this approach the accurate field below the line can be evaluated along

with the associate input impedance of a possible probe excitation. Also, the scattering at the edges yields its radiation impedance, the leaked energy, as well as its radiated field, e.g., [36]. But the specific case studied herein can be best exploited for the analysis of rectangular patch antennas printed on solid state plasma, where the internal waves (below the patch) are almost normally incident at the two of its four edges, e.g., [34, 36]. The value of the present Wiener-Hopf analysis can be understood as offering physical insight into the involved scattering phenomena and consequently providing the means to optimize or tune the radiated field [34]. Unique and exotic radiating structures can be built exploiting the involved tunable unidirectional waves supported by the studied structure. A similar example from magnetized ferrites is a tunable travelling wave antenna which includes a build-in circulator, i.e., the forward unidirectional wave is activated in transmit and the back-propagating one for receive functions [29]. Many attractive features of proposed anisotropic slabs in the band of optical frequencies are noticed in the work of Taya [39–42]. There the effect of anisotropy in the refractive index enables the slab to act as sensor, which can "be used in the characterization of plasma media" [39]. Increasing the mode's wavelength or decreasing substrate's thickness causes the sensitivity of the sensor to increase [39]. This is of primary importance, since these sensors can be used in biomedical applications [39, 41]. Moreover, their use is also extended in the field of radiating structures, such as the proposed antenna structures of Huang et al. [43]. These antennas, operating in the two main communication bands of WLAN, (2.4–2.4835 GHz), and WiMAX, (3.3 GHz), are realized based on solid state plasma materials. These antenna configurations have the special advantages of small volume, low profile, easy to carry, convenient real time control, and almost perfect directivity, especially in the WLAN band [43]. Hence, the analysis presented herein offers the means and primarily the physical insight to devise novel and unique microwave front end stages including antennas.

This paper is organized as follows. Section 2 recalls the characteristic equation and the formulation of the Wiener-Hopf equation for the grounded anisotropic plasma. Section 3 presents the factorization procedure of the resulting Kernel function. The Kernel function is first decomposed into a symmetrical even and a non-even term. Then, the expressions for the reflection coefficient, as well as integral equations describing the scattered field, are derived. Residues of poles of these integral equations determine the contribution of both surface and leaky waves to the scattered field. Section 4 shows the resulting dispersion curves for both surface and leaky waves excited in the anisotropic plasma slab. The field of unidirectional waves is studied next as well as the dependence of these waves turn-on conditions from the plasma tensor entries. Finally, a steepest descent method is employed in order to evaluate the far field radiation. Field radiation is evaluated and plotted as a function of magnetizing dc field and the waveguide thickness for validations purposes. For the sake of brevity, we have omitted several mathematical proofs that the reader can find in [8–18].

2. FORMULATION OF THE CANONICAL PROBLEM AND WIENER-HOPF EQUATIONS

As noted in the introduction, this work constitutes an extension of our previous work [9], toward the evaluation of the scattered near and/or far field when the structure is open-radiating. The study, when the structure is shielded, is carried out in [9] along with the formulation of the Wiener-Hopf equation for both shielded and open cases. In order for this paper to be self-sustained a synopsis of formulation [9] will be tried first.

The geometry to be studied is shown in Fig. 1. Basically, it consists of a parallel plane waveguide loaded with magnetized plasma, where the lower conductor (ground plane) and the plasma substrate are assumed extending to infinity, while a semi-infinite (truncated, $z < 0$) upper conductor is considered. The biasing constant magnetic field ($\overline{H}_{dc}$) is assumed parallel to the two planes and parallel to the edge, ($\hat{y}$-axis, $\overline{H}_{dc} = H_0\hat{y}$), of the truncated plane conductor. The extra-ordinary TEM wave (possibly emanating from a probe feed) propagating in the parallel plane region along the $\hat{z}$-axis (transverse to $\overline{H}_{dc}$) is considered to be incident normally on the edge defined by the truncated upper conductor. The open structure of the parallel plane waveguide is presented in Fig. 1(b), as well as the shielded structure in Fig. 1(a). Time harmonic fields ($e^{j\omega t}$) and a spatial ($\hat{z}$-axis) to a λ-space (propagation constants)
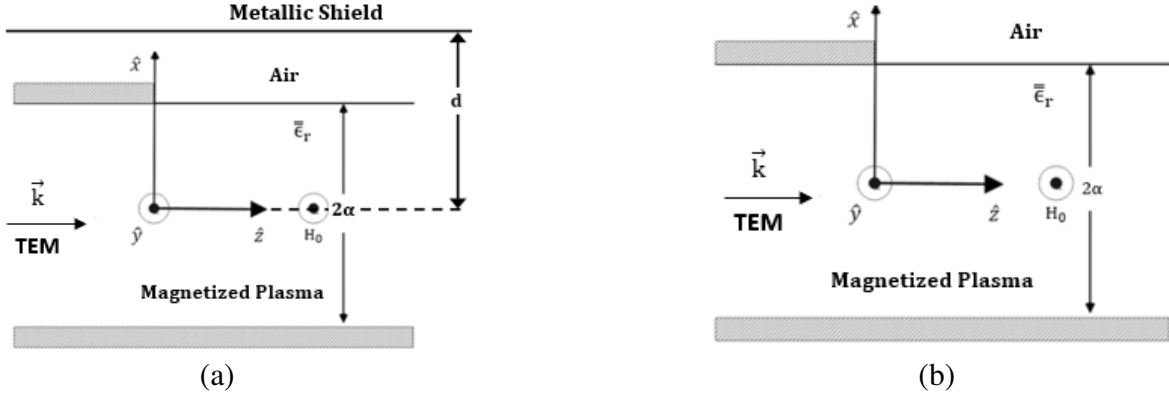
Figure 1. A TEM wave incident upon the edge defined by the truncated upper conductor of a parallel plane waveguide loaded with longitudinally magnetized plasma. Wave propagation normal to the biasing DC magnetic field is considered (a) shielded geometry, (b) open geometry.

spectrum Fourier transform pair is considered (in the form $e^{jk_0\lambda \cdot z}$) as follows:

$$\tilde{f}(\lambda) = \frac{k_0}{2\pi}\left\{\int_{-\infty}^{0} + \int_{0}^{\infty}\right\} f(z)e^{jk_0\lambda\cdot z}dz = \tilde{f}_-(\lambda) + \tilde{f}_+(\lambda) \tag{1}$$

and the inverse Fourier transform:

$$f_+(z) = \begin{cases} \int_{+\infty} \tilde{f}_+(\lambda)e^{-jk_0\lambda z}d\lambda, & \text{for } z \geq 0 \\ 0, & \text{for } z < 0 \end{cases}, \quad f_-(z) = \begin{cases} 0, & \text{for } z > 0 \\ \int_{-\infty} \tilde{f}_-(\lambda)e^{-jk_0\lambda z}d\lambda, & \text{for } z \leq 0 \end{cases} \tag{2a}$$

The spectral functions $\tilde{f}_-(\lambda)$ and $\tilde{f}_+(\lambda)$ are analytic in the lower and upper λ half-planes respectively, hence are called "negative" and "positive" functions. On the other hand, the spatial functions $f_+(z)$ and $f_-(z)$ are defined only in the positive and negative z half-planes according to Eq. (2a), and their summation gives the total response.

$$f(z) = f_-(z) + f_+(z) \tag{2b}$$

As shown in Fig. 2, the contour C_+ must be closed in the lower λ half-plane when $f_+(z)$ for $z > 0$ will be recovered employing Cauchy's formula. Likewise, when $f_-(z)$ for $z < 0$ is to be recovered, the integration contour C_- must be closed in the upper λ half-plane. Note only this selection of contours ensures that the integrands will tend to zero at infinity, $(|z| \rightarrow \infty)$, or equivalently that the associated field expressions will obey the radiation condition at infinity (assuming the presence of at least small losses).

The Fourier transform pair of Eqs. (1), (2) yields the same simplification as when considering wave propagation along the z-axis like $e^{-jk_0\lambda z}$ namely to substitute $\frac{\partial}{\partial z} = -jk_0\lambda$. For further simplification, the analysis is restricted to the case without variation of the scattered field in the also infinite y-direction, resulting to the simplification $\frac{\partial}{\partial y} = -jk_y = 0$. Moreover, the magnetized cold plasma ($\overline{H}_{\rm dc} = H_0\hat{y}$) relative permittivity tensor is also given in [5] and the original references cited herein and in [8] as:

$$\overline{\overline{\epsilon}}_r = \begin{bmatrix} \epsilon_{r1} & 0 & j\epsilon_{r2} \\ 0 & \epsilon_{r3} & 0 \\ -j\epsilon_{r2} & 0 & \epsilon_{r1} \end{bmatrix} \text{ where } \epsilon_{r1} = \frac{\Omega^2 - R^2 - 1}{\Omega^2 - R^2}, \quad \epsilon_{r2} = \frac{R}{\Omega(\Omega^2 - R^2)}, \quad \epsilon_{r3} = 1 - \frac{1}{\Omega^2} \tag{3a}$$

and

$$\Omega = \frac{\omega}{\omega_p}, \ R = \frac{\omega_c}{\omega_p}, \ \omega_p^2 = \frac{Ne^2}{m\epsilon_0} = \frac{\gamma Ne}{\epsilon_0}, \ \omega_c = -\frac{e\mu_0 H_0}{m} = -\gamma\mu_0 H_0 \tag{3b}$$

The above parameters ω_p and ω_c symbolize the plasma and gyromagnetic circular frequency, respectively. The normalized gyromagnetic frequency is symbolized as R. Also, e and m are the
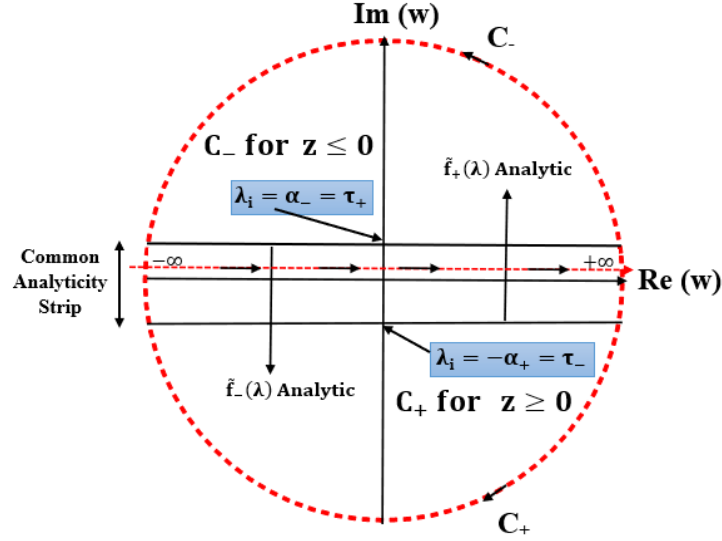
Figure 2. Definitions of $\tilde{f}_+(\lambda)$ and $\tilde{f}_-(\lambda)$ analyticity regions and the appropriate C_+, C_- integration contours.

charge and mass of an electron; $\gamma = \frac{q}{m}$ is the magneto-mechanic or gyroelectric ratio; ϵ_0, μ_0 are the free space permittivity and permeability; N is the average density of electrons.

In the geometry of the problem, shown in Fig. 1, the region $-\infty < z < +\infty$, $-\infty < y < +\infty$, and $-\alpha < x < \alpha$ is filled with uniform magnetized plasma, and the rest of half-space $x > \alpha$ is vacuum. The wave equation for the scattered magnetic field in the plasma region $-\alpha \leq x \leq \alpha$ can be written as [8, 12]:

$$\left[\frac{\partial^2}{\partial x^2} + k_0^2 \left(\frac{\epsilon_{rq}}{\epsilon_{r1}} - \lambda^2 \right) \right] \tilde{H}_y^s = 0 \tag{4}$$

where $k_0 = \omega\sqrt{\mu_0 \epsilon_0}$ the free space wavenumber, $\epsilon_{rq} = \epsilon_{r1}^2 - \epsilon_{r2}^2$, and the transverse effective permittivity is $\epsilon_{r\,\text{eff}} = \frac{\epsilon_{rq}}{\epsilon_{r1}}$. The general solution of Eq. (4) takes the form:

$$\tilde{H}_y^s = B_p(\lambda)\cosh\left(k_0 u_p x\right) + C_p(\lambda)\sinh\left(k_0 u_p x\right) \ \ \text{for} \ -\alpha \leq x \leq \alpha \tag{5a}$$

where:

$$u_p = \sqrt{\lambda^2 - \epsilon_{r\,\text{eff}}} = \sqrt{\lambda^2 - \frac{\epsilon_{rq}}{\epsilon_{r1}}} \ \ \text{and} \ \ \text{Re}(u_p) \geq 0 \tag{5b}$$

In order to ensure attenuated waves in the presence of losses only solutions with $\text{Re}(u_p) \geq 0$ are acceptable. The transverse field components can also be expressed by expanding the Maxwell rotational equations and using the above simplifications [9]:

$$\tilde{E}_x^s = \frac{\zeta_0}{\epsilon_{rq}}\left\{ \lambda\epsilon_{r1}\tilde{H}_y^s - \frac{\epsilon_{r2}\partial\tilde{H}_y^s}{k_0\partial x} \right\} \ \ \text{and} \ \ \tilde{E}_z^s = j\frac{\zeta_0}{\epsilon_{rq}}\left\{ \lambda\epsilon_{r2}\tilde{H}_y^s - \frac{\epsilon_{r1}\partial\tilde{H}_y^s}{k_0\partial x} \right\} \tag{6}$$

where $\zeta_0 = \sqrt{\mu_0/\epsilon_0} = 120\pi\,\Omega$ is the free space characteristic impedance.

The solution in the air region must obey the radiation condition at infinity taking the form:

$$\tilde{H}_y^s = A_p(\lambda)\cdot e^{-k_0 u_0 (x-\alpha)} \ \ \text{for} \ x \geq \alpha \tag{7a}$$

$$\text{with} \ u_0 = \sqrt{\lambda^2 - 1} \ \ \text{and} \ \ \text{Re}(u_0) \geq 0 \tag{7b}$$

$$\tilde{E}_x^s = -\frac{1}{j\omega\epsilon_0}\frac{\partial\tilde{H}_y^s}{\partial z} = \zeta_0 \cdot \lambda \cdot \tilde{H}_y^s \ \ \text{and} \ \ \tilde{E}_z^s = \frac{1}{j\omega\epsilon_0}\frac{\partial\tilde{H}_y^s}{\partial x} = j\zeta_0 u_0 \cdot \tilde{H}_y^s \tag{8}$$

The spectral quantities $B_p(\lambda)$ and $C_p(\lambda)$ can be obtained in terms of $A_p(\lambda)$ by imposing the boundary conditions and are explicitly defined as:

$$B_p(\lambda) = \frac{\epsilon_{rq} u_0 A_p(\lambda)}{2\left[(\lambda\epsilon_{r2})^2 - (\epsilon_{r1} \cdot u_p)^2\right]} \cdot \left(\frac{\lambda\epsilon_{r2}}{\cosh(k_0 u_p \alpha)} + \frac{\epsilon_{r1} \cdot u_p}{\sinh(k_0 u_p \alpha)}\right) \tag{9}$$

$$C_p(\lambda) = \frac{\epsilon_{rq} u_0 A_p(\lambda)}{2\left[(\lambda\epsilon_{r2})^2 - (\epsilon_{r1} \cdot u_p)^2\right]} \cdot \left(\frac{\epsilon_{r1} \cdot u_p}{\cosh(k_0 u_p \alpha)} + \frac{\lambda\epsilon_{r2}}{\sinh(k_0 u_p \alpha)}\right) \tag{10}$$

The common term in Eqs. (9)–(10) can be simplified as:

$$\frac{\epsilon_{rq}}{2\left[(\lambda\epsilon_{r2})^2 - (\epsilon_{r1} \cdot u_p)^2\right]} = \frac{-1}{2(\lambda^2 - \epsilon_{r1})} \tag{11}$$

The incident extra-ordinary TEM wave propagating in the parallel-plane region toward the positive z-direction is given by Johansen [12], or Bates and Mittra [8], in the spatial domain as:

$$H_y^i = \exp\left(\frac{k_0 \epsilon_{r2} x}{\sqrt{\epsilon_{r1}}} - jk_0\sqrt{\epsilon_{r1}}z\right) \text{ and } E_x^i = \frac{\zeta_0}{\sqrt{\epsilon_{r1}}} \cdot H_y^i \tag{12}$$

The inhomogeneous boundary conditions at the interface $x = \alpha$ (truncated metal-air for $z < 0$ and plasma-air for $z > 0$) are imposed, and the Jones' procedure [14] is followed to formulate the Wiener-Hopf equation in [9]:

$$Q(\lambda)\tilde{R}_+(\lambda) = \tilde{L}_-(\lambda) - \tilde{j}_+^i(\lambda) \tag{13}$$

The involved spectral current density $\tilde{j}_+^i(\lambda)$ results from a fictitious but mathematically rigorous and convenient induced current density on the plasma-air interface ($x = \alpha, z > 0$), according to Mittra and Lee [14, p. 126]. For this assumption, the incident field is assumed to propagate un-attenuated beyond the edge in the region $z > 0$. The fictitious field contribution introduced in the scattered field will be evaluated from its residue and subtracted later on. Since this current density is identically zero at the interface, ($x = \alpha, z > 0$), it can be represented by a "positive" function as:

$$\tilde{j}_+^{\cdot i}(\lambda) = -\frac{k_0}{2\pi}\int_0^\infty H_y^i\left(x = \alpha^-, z\right)e^{jk_0\lambda z}dz = -j\frac{1}{2\pi(\lambda - \sqrt{\epsilon_{r1}})} \cdot \exp\left(k_0\epsilon_{r2}\alpha/\sqrt{\epsilon_{r1}}\right), \text{ valid for } z > 0 \tag{14}$$

The vanishing electric field on the boundary condition on the semi-infinite metallic upper conductor ($x = \alpha, z < 0$) is satisfied through a "positive" spectral function as [9]:

$$\tilde{R}_+(\lambda) = u_0 A_p(\lambda) \tag{15}$$

On the contrary, the tangential magnetic field (H_y) exhibits an unusual discontinuity at the semi-infinite plasma-air interface, ($x = \alpha, z > 0$), equal to the fictitious current density $\tilde{j}_+^i(\lambda)$. This is in turn ensured through the definition of a "negative" spectral function, as in [9]:

$$\tilde{L}_-(\lambda) = \tilde{H}_y^s\left(x = \alpha^+, \lambda\right) - \tilde{H}_y^s\left(x = \alpha^-, \lambda\right) + \tilde{j}_+^i(\lambda) \tag{16}$$

The Kernel $Q(\lambda)$ reads:

$$Q(\lambda) = \frac{1}{u_0} + \frac{\lambda\epsilon_{r2} + \epsilon_{r1} \cdot u_p \cdot \coth(2k_0 u_p \alpha)}{(\lambda^2 - \epsilon_{r1})} \tag{17}$$

The inverse function G of the Kernel that is used in next Sections, is explicitly defined in Eq. (19), as a product of expressions (20)–(22). $Q(\lambda) = 0$ is identified as the characteristic equation of the open problem and needs to be factorized as its roots constitute the propagation constants of the excited modes. Additionally, the corresponding Kernel function for the shielded geometry of Fig. 1(a) studied analytically in [9] is defined as:

$$Q_{\text{closed}}(\lambda) = \frac{1}{u_0 \tanh[k_0 u_0(d - \alpha)]} + \frac{\lambda\epsilon_{r2} + \epsilon_{r1} u_p \coth(2k_0 u_p \alpha)}{\lambda^2 - \epsilon_{r1}} \tag{18}$$

It is obvious from Eq. (18) that in the limit when the metallic shield distance is moved to infinity $d \to \infty$, the term $\tanh[k_0 u_0(d - \alpha)]$ tends to unity, and the above equation yields the respective one, Eq. (16) for the open geometry.

3. FACTORIZATION OF KERNEL FUNCTION G

For the solution of the Wiener-Hopf equation, the Kernel function in Eq. (17) must be separated into "positive" and "negative" terms. For this purpose, Kernel $Q(\lambda)$ or its inverse $G(\lambda)$ should be factorized into a product as: $Q(\lambda) = Q_+(\lambda) \cdot Q_-(\lambda)$ or $G(\lambda) = 1/Q(\lambda) = G_+(\lambda) \cdot G_-(\lambda)$. The challenge here is to handle the anisotropy introduced by the permittivity tensor in Eq. (3a) and particularly the term $\lambda \epsilon_{r2}$ which causes the kernel in Eq. (17) to lose their even symmetry. Physically, this is reflected to the non-reciprocal behavior of the magnetized plasma, which in turn causes waves propagating in the positive and negative z-direction to have different propagation constants. Although there is a plethora of publications elaborating on the factorization of the classical even Kernels (referred to isotropic media), there are only a few for non-even functions. To our knowledge the only general one is that of Fikioris et al. [16], which handles a similar structure loaded with magnetized ferrite material. Their technique is modified herein for the magnetized plasma loading. The authors in [16] manipulated the Kernel functions and were able to extend the general factorization technique developed by Bates and Mittra [15], for adapt even-functions. The extension of [16] was able to adapt this technique to non-even Kernels' factorization. Herein, the Kernel $G(\lambda)$ is first expressed in terms similar to [16] as:

$$G(\lambda) = g(\lambda) G_1(\lambda) G_2(\lambda) \tag{19}$$

where

$$g(\lambda) = 2k_0 \alpha (\lambda^2 - \epsilon_{r1}) \tag{20}$$

$$G_1(\lambda) = \frac{\sinh(2k_0 u_p \alpha)}{2k_0 \alpha u_p} \tag{21}$$

$$G_2(\lambda) = \frac{u_0 u_p}{[\lambda^2 - \epsilon_{r1} + \lambda \epsilon_{r2} u_0] \sinh(2k_0 u_p \alpha) + \epsilon_{r1} u_0 u_p \cosh(2k_0 u_p \alpha)} \tag{22}$$

Namely, the original function $G(\lambda)$ is written as a product of a usual even function $G_1(\lambda)$ and a non-even $G_2(\lambda)$ similar to that of [16]. The Kernel function described by Eq. (22) involves a non-even and non-reciprocal term $\lambda \epsilon_{r2}$ resulting from the plasma anisotropy. The ordinary even function $G_1(\lambda)$ is factorized as in [10], while for the non-even function $G_2(\lambda)$ the Fikioris et al. technique [16] is adopted. A comparison of the Kernels of the ferrite structure of [16], its dual and the one studied herein is given in Table 1. The structure of Fikioris et al. [16] assumed a magnetized ferrite loading, excited by a TE$_{n0}$ mode. Although the dual structure transformed through the duality principle to that of magnetized plasma loading, the involved boundaries become perfect magnetic conductors (PMC), while the excitations is by TM$_{n0}$ modes. On the contrary, herein we aim at structures printed on a semiconductor substrate, which at cryogenic temperatures exhibit magnetized plasma properties when biased by a DC magnetic field. Thus, the studied structure of Fig. 1(b) involves perfect electric conductor (PEC), boundarie and the excitation by a TEM mode in order to allow for electrically thin substrates. Indeed, the dual structure exhibits the same mathematical form as that of [16], and its Kernel could be readily factorized as in [16]. However, the structure elaborated herein has a different first term in the denominator of the non-symmetric function $G_2(\lambda)$. Hence, this factorization must be reestablished following a similar mathematical approach as in [16]. Modes excited are of type E-modes, as described in [9]. The lowest order surface mode is a TEM wave ($\lambda = \sqrt{\epsilon_{r1}}$), similar to [12], with its behavior affected by ϵ_{r2} as described later in Tables 4 and 5.

3.1. Factorization of Even Function G_1

As G_1 is concerned, it is a meromorphic even function of λ and can be factorized almost by inspection [14, Sec. 3-6(3), p. 91], leading to the factors $G_1(\lambda) = G_{1+}(\lambda) G_{1-}(\lambda)$:

$$G_1(\lambda) = G_1(0) \prod_{n=1}^{\infty} \left(1 + \frac{\lambda}{j\gamma_n}\right) \exp\left(+\frac{jk_0 \lambda 2\alpha}{n\pi}\right) \prod_{n=1}^{\infty} \left(1 - \frac{\lambda}{j\gamma_n}\right) \exp\left(-\frac{jk_0 \lambda 2\alpha}{n\pi}\right) \tag{23}$$

which yields:

$$G_{1\pm}(\lambda) = \sqrt{G_1(0)} \prod_{n=1}^{\infty} \left(1 \mp \frac{\lambda}{j\gamma_n}\right) \exp\left(\mp \frac{jk_0 \lambda 2\alpha}{n\pi}\right) \tag{24}$$

Table 1. Definition of variables and functions in Fikioris' [16], and present problems.

	Fikioris' Problem	Present Problem
Time Dependence	$\exp(-j\omega t)$	$\exp(+j\omega t)$
Anisotropic Entries	$\overline{\overline{\mu}}_r, \mu_{r1}, \mu_{r2}, \mu_{r3}, \mu_{reff}$	$\overline{\overline{\epsilon}}_r, \epsilon_{r1}, \epsilon_{r2}, \epsilon_{r3}, \epsilon_{reff}$
Incident Wave	TE_{n0}	Extra-Ordinary TEM
Infinite Axis Assumed Independent Field	$\hat{y}$-axis	$\hat{y}$-axis
Field Excited Components	H_x, H_z, E_y	E_x, E_z, H_y
Propagation Constant	u	λ
Tangential Wavenumber Inside Slab's Material	τ_2	u_p
Tangential Wavenumber in Air Region	$\gamma_0 = \sqrt{u^2 - k_0^2}$	$u_0 = \sqrt{\lambda^2 - 1}$
Transforming Variable	β	w
Waveguide Height	d	2α
Functions	$A_\pm, F, M_\pm, K_\pm, P$	$A_\mp, F, M_\mp, K_\mp, X$
Asymptotic Form of G_{1+}	$u^{-\frac{1}{2}} e^{-\frac{jud}{\pi}} \left[1 - \gamma - \ln\left(-j\frac{ud}{\pi}\right)\right]$	$\lambda^{-\frac{1}{2}} e^{\frac{jk_0\lambda 2\alpha}{\pi}} \left[1 - \gamma - \ln\left(\frac{jk_0\lambda 2\alpha}{\pi}\right)\right]$
Asymptotic Form of G_2	$\dfrac{e^{-du\,\mathrm{sgn}(\mathrm{Re}(u))}}{\mu_1 + (\mu_1^2 - \mu_2^2) - \mu_2 \mathrm{sgn}(\mathrm{Re}(u))}$	$\dfrac{\frac{1}{2} e^{-2k_0\lambda\,\mathrm{sgn}(\mathrm{Re}(\lambda))\alpha}}{1 + \mathrm{sgn}(\mathrm{Re}(\lambda))\epsilon_{r2} + \epsilon_{r1}}$

where $\gamma_n = j\sqrt{\epsilon_{reff} - \left(\frac{n\pi}{2\alpha}\right)^2}$ and $G_1(0) = \frac{\sin(2k_0\alpha\sqrt{\epsilon_{reff}})}{2k_0\alpha\sqrt{\epsilon_{reff}}} = \mathrm{sinc}(2k_0\alpha\sqrt{\epsilon_{reff}})$.

From the above expression (24) the even symmetry as $G_{1-}(\lambda) = G_{1+}(-\lambda)$ is justified. Using the approximations of [14, Sec. 3.6.(3)], in order to define the asymptotic form of (24), Kernel function G_1 is defined as:

$$G_{1+}(\lambda)\Big|_{|\lambda| \to \infty} \sim \lambda^{-\frac{1}{2}} \exp\left(\frac{jk_0\lambda 2\alpha}{\pi}\left[1 - \gamma - \ln\left(\frac{jk_0\lambda 2\alpha}{\pi}\right)\right]\right) \tag{25}$$

where $\gamma = 0.57721$ Euler's constant.

3.2. Factorization of Non-Even Function G_2

On the contrary, the factorization of G_2 is much more complicated. Exactly as in the isotropic case [7], a first difficulty arises from the open character of the present structure which is responsible for the presence of a branch cut in the expression of G_2 due to the double valued function u_0. As a prerequisite of this procedure, the factorization method developed by Bates and Mittra [15] is extended to the present non-symmetric case. Note that the G_2 term of the current work is similar but more complex than the one studied by Fikioris et al. [16].

In the present non-symmetric Kernel problem, the same method developed by Fikioris et al. [16] is applied. As mentioned in [15], the two $(+)$ and $(-)$ factors of G_2 function can be represented by the following expressions:

$$G_{2\pm}(\lambda) = \sqrt{G_2(0)} \exp\left(A_\pm(\lambda) + hM_\pm(\lambda) + \frac{jk_0h}{2}\right) \tag{26}$$

$$G_2(0) = \frac{\sqrt{\epsilon_{reff}}}{j\epsilon_{r1}\sin\left(2k_0\alpha\sqrt{\epsilon_{reff}}\right) + \epsilon_{r1}\sqrt{\epsilon_{reff}}\cos\left(2k_0\alpha\sqrt{\epsilon_{reff}}\right)} \tag{27}$$

$$A_\pm(\lambda) = \pm\frac{1}{2\pi j}\int_{-\infty\pm jh}^{+\infty\pm jh} \frac{\lambda F(w)}{w(w-\lambda)}\,dw, \quad \tau_- < -h < \tau < h < \tau_+ \tag{28}$$

$$F\left(\lambda\right) = hu_0 + \ln G_2\left(\lambda\right) \tag{29}$$

The integration contour is depicted in Fig. 2, and h stands for the limit of Kernel function G_2 in terms of $\exp(-hk_0\lambda)$ [14, p. 114], as λ tends to infinity, and functions $M_\pm(\lambda)$ denote the decomposition terms on C_+ and C_- complex half domains. Because of the differences between the present non-symmetric function G_2 and the one studied in [16], each term in Eq. (26) should be defined explicitly. The above definitions are encountered in the literature [14, 15], denoted in the opposite sense of j. This is due to the opposite signs in the field time dependence assumed [19]. The correspondence of variables and functions utilized in [16] to those employed herein are depicted in Table 1, in order to track the changes.

First the asymptotic behavior as of Kernel function G_2 is studied, in order to identify factor h. So,

$$G_2\left(\lambda\right)\Big|_{|\lambda| \to \infty} \approx \frac{\dfrac{1}{2}e^{-2k_0\lambda\,\mathrm{sgn}(\mathrm{Re}(\lambda))\alpha}}{1 + \mathrm{sgn}(\mathrm{Re}\left(\lambda\right))\epsilon_{r2} + \epsilon_{r1}} \propto C^\nu e^{-k_0\lambda h} \tag{30}$$

with $\nu = 0$ and $h = 2\alpha$ being the substrate thickness in Fig. 1. Functions $M_\pm(\lambda)$ denote the decomposition terms defined through the relation:

$$k_0 u_0\left(\lambda\right) = M_+\left(\lambda\right) + M_-\left(\lambda\right) \tag{31}$$

Although Eq. (31) seems identical to that of [16] for γ_0, there is a major difference due to the temporal $\exp(-j\omega t)$ assumption therein. Thus, the correspondence to $(+)$ or $\mathrm{Im}(\lambda) > 0$ and $(-)$ or $\mathrm{Im}(\lambda) < 0$ is interchanged.

After some algebraic manipulations working according to Noble [17, p. 21], Daniele [18, Ch. 1.3.1 p. 6], or Fikioris et al. [16], the decomposition yields:

$$M_\pm\left(\lambda\right) = \frac{k_0 u_0}{\pi}\cos^{-1}\left(\mp\lambda\right) = \frac{k_0 u_0}{\pi j}\ln\left(\mp\lambda + u_0\right) = \mp\frac{k_0 u_0}{2\pi j}\ln\left(\frac{\lambda + u_0}{\lambda - u_0}\right) \tag{32}$$

Its null argument is obtained setting $\lambda = 0$ in Eq. (32):

$$M_+\left(0\right) = M_-\left(0\right) = \frac{k_0 u_0\left(0\right)}{2} \tag{33}$$

As stated in [16] expressing λ and u_0 in terms of distances ρ_1 and ρ_2 from branch points in a similar sense to [16], in order to yield a more concrete representation of functions M_+ and M_-. The defined angles φ_1 and φ_2 are in the opposite sense of [16] in order to retain $\mathrm{Re}(u_0) \geq 0$ for the $\exp(+j\omega t)$ temporal dependence. Writing the propagation constant as $\lambda = r \cdot \exp(j\theta)$ and recalling formulas from [20, p. 80–81], the approach in [16] yields:

$$R_\pm = \left\{r^2 + \rho_1\rho_2 \pm 2r\sqrt{\rho_1\rho_2}\cos\left(\frac{\varphi_1 + \varphi_2}{2} - \theta\right)\right\}^{\frac{1}{2}} \tag{34a}$$

$$\Psi = \tan^{-1}\left[\frac{2r\sqrt{\rho_1\rho_2}\sin\left(\dfrac{\varphi_1 + \varphi_2}{2} - \theta\right)}{r^2 - \rho_1\rho_2}\right] \tag{34b}$$

Decomposed functions M_+ and M_- are defined in Table 2 and compared with the respective ones of [16]. Because functions $A_\pm(\lambda)$ in Eq. (28) are in a very complicated form and difficult to be evaluated, the technique of integration by parts developed by Bates and Mittra [15] is adapted by Fikioris et al. [16], for the non-symmetric case. This is also followed herein, since it leads to a more concrete form of $G_{2\pm}(\lambda)$.

$$G_{2\pm}\left(\lambda\right) = \sqrt{G_2\left(0\right)}\left(1 \pm \lambda\right)^{\frac{\nu}{2}}\exp\left(j\alpha k_0 + 2\alpha M_\pm(\lambda) + A_\pm\left(\lambda\right)\right) \tag{35a}$$

or equivalently:

$$G_{2\pm}\left(\lambda\right) = \sqrt{G_2\left(0\right)}\left(1 \pm \lambda\right)^{\frac{\nu_1}{2}}\prod_{n=1}^{N}\left(1 \mp \frac{\lambda}{\eta_{n\pm}}\right)^{-1}\exp\left(j\alpha k_0 + 2\alpha M_\pm(\lambda) + T_\pm\left(\lambda\right)\right) \tag{35b}$$

where $G_2(0)$ is defined by Eq. (27); $A_\pm(\lambda)$ is defined by Eq. (28); and $\eta_{n\pm}$ denote the roots of the equations $[\lambda^2 - \epsilon_{r1} \pm \lambda\epsilon_{r2}u_0]\sinh(2k_0 u_p\alpha) + \epsilon_{r1}u_0 u_p\cosh(2k_0 u_p\alpha)$, respectively. Following a similar

Table 2. Comparison of decomposed functions between plasma and ferrite [16], problems.

Structure	Decomposition Function M_+
Fikioris [16] Ferrite	$M_+(\lambda) = \frac{1}{2\pi j}\sqrt{\rho_1\rho_2}\, e^{\frac{j(\varphi_1+\varphi_2)}{2}} \left[\ln\frac{R_+}{R_-} + j\Psi\right]$
Present Plasma	$M_+(\lambda) = -\frac{1}{2\pi j}\sqrt{\rho_1\rho_2}\, e^{\frac{j(\varphi_1+\varphi_2)}{2}} \left[\ln\frac{R_+}{R_-} + j\Psi - j2\pi\right]$
	Decomposition Function M_-
Fikioris [16] Ferrite	$M_-(\lambda) = -\frac{1}{2\pi j}\sqrt{\rho_1\rho_2}\, e^{\frac{j(\varphi_1+\varphi_2)}{2}} \left[\ln\frac{R_+}{R_-} + j\Psi + j2\pi\right]$
Present Plasma	$M_-(\lambda) = \frac{1}{2\pi j}\sqrt{\rho_1\rho_2}\, e^{\frac{j(\varphi_1+\varphi_2)}{2}} \left[\ln\frac{R_+}{R_-} + j\Psi\right]$

procedure to [16], the $+\lambda\epsilon_{r2}u_0$ is used for the positive functions, with the term $-\lambda\epsilon_{r2}u_0$ for the negative functions.

The above functions yield $T_\pm(\lambda)$ which is involved in Eq. (35) as [11, 15]:

$$T_\pm(\lambda) = \int_0^\infty K_\pm(w)\ln\left[1 \pm \frac{\lambda}{(1-w^2)^{\frac{1}{2}}}\right] dw \tag{36a}$$

The function $K_+(w)$ can be defined as:

$$K_+(w) = \frac{2\alpha}{\pi} + \frac{1}{2\pi j}\left(B_+(w) + B_+(-w)\right) \Rightarrow$$

$$K_+(w) = \frac{2\alpha}{\pi} + \frac{1}{2\pi j}\frac{H_+\left(\sqrt{1-w^2}\right)G_2\left(-\sqrt{1-w^2}\right) - H_+\left(-\sqrt{1-w^2}\right)G_2\left(\sqrt{1-w^2}\right)}{G_2\left(\sqrt{1-w^2}\right)G_2\left(-\sqrt{1-w^2}\right)} \tag{36b}$$

The functions B and H involved in Eq. (36b) are defined in [8, 14] and are evaluated as [11, 15]:

$$B_\pm(w) = \frac{H_\pm\left(\sqrt{1-w^2}\right)}{G_{2\pm}\left(\sqrt{1-w^2}\right)} \tag{36c}$$

with

$$H\left(\sqrt{1-w^2}\right) = \frac{d}{dw}\left(G_2\left(\sqrt{1-w^2}\right)\right) \tag{36d}$$

Imposing $\lambda = \pm\sqrt{1-w^2}$ on Eq. (22) yields the term $G_2(\pm\sqrt{1-w^2})$. A complicated mathematical manipulation is needed for the evaluation of $K_\pm$ through Eq. (36c). The symbolic feature of Mathematica [21] is employed, which after multiple "simplification" iterations yields the final expression as:

$$B_+(\pm w) = \left\{ j2\alpha k_0 w^2\tau_0\tau_p\left(1-\epsilon_{r1} - w^2 \pm j\epsilon_{r2}w\tau_0\right)\cos\left(2\alpha k_0\tau_p\right) \right.$$

$$\left. + \left[j\tau_0\left[w^4 + (\epsilon_{r1}-1)\tau_p^2 - w^2\left(\tau_p^2 - \epsilon_{r1} + 1\right)\right] \pm w^3\left(\epsilon_{r2}\tau_0^2 + \epsilon_{r2}\tau_p^2 + 2\alpha k_0\epsilon_{r1}\tau_0\tau_p^2\right)\right]\sin\left(2\alpha k_0\tau_p\right) \right\}$$

$$\left\{ \pm w\tau_0\tau_p^2\left[\pm\epsilon_{r1}w\tau_p\cos\left(2\alpha k_0\tau_p\right) + \left(\pm\epsilon_{r2}w\tau_0 + jw^2 + j\epsilon_{r1} - j\right)\sin\left(2\alpha k_0\tau_p\right)\right]\right\}^{-1} \tag{36e}$$

where:

$$\tau_p = \sqrt{w^2 + \epsilon_{reff} - 1} \quad \text{and} \quad \tau_0 = \sqrt{1-w^2} \tag{36f}$$

The result for $\nu = 0$ obtained in Eq. (30) is similar to [16]. On the opposite, ν_1 in Eq. (35b) using Mathematica [21] yields:

$$\nu_1 = \lim_{w\to 0} wB_\pm(w) = 1 \tag{36g}$$

Negative $(-)$ expressions of (36a)–(36f) yield the same with positive $(+)$, except of an opposed sign in front of ϵ_{r2}, resulting from the initial assumption of negative term $-\lambda\epsilon_{r2}u_0$. Although Eq. (36d) is a complicated expression as far as mathematical interpretation is concerned, it is however convenient for numerical computation purposes. Substituting back to Eq. (35), the final expression for $G_\pm(\lambda)$ reads:

$$G_\pm(\lambda) = (\lambda \mp \sqrt{\epsilon_{r1}})(1 \pm \lambda)^{\frac{1}{2}} \sqrt{G(0)} \prod_{n=1}^{\infty} \prod_{m=1}^{M} \frac{\left(1 \mp \dfrac{\lambda}{j\gamma_n}\right)}{\left(1 \mp \dfrac{\lambda}{\eta_{m\pm}}\right)}$$

$$\cdot \exp\left[\frac{\pm j2k_0\lambda\alpha}{n\pi} + j\alpha k_0 + 2\alpha M_\pm(\lambda) + T_\pm(\lambda) \pm X(\lambda)\right] \tag{37}$$

where $G(0) = -2k_0\alpha\epsilon_{r1}G_1(0)G_2(0)$ from Eq. (19).

The new term in Eq. (37), $X(\lambda)$ is an entire function which must be included so as to ensure the algebraic behavior of $G_\pm(\lambda)$ at infinity, (as $|\lambda| \to \infty$). For this purpose, it is necessary to estimate its asymptotic behavior, which is similar to [18, Ch. 1.3.1]:

$$G_{2+}(\lambda)\Big|_{|\lambda| \to \infty} \approx \exp\left(\frac{j2\alpha k_0\lambda}{\pi}\ln(-2\lambda)\right) \tag{38}$$

The entire function $X(\lambda)$ yields:

$$X(\lambda) = \frac{-jk_0\lambda 2\alpha}{\pi}\left[1 - \gamma + \ln\left(\frac{\pi}{k_0\alpha}\right) + \frac{j\pi}{2}\right] \tag{39}$$

By means of Eqs. (37)–(39) and (36d)–(36f) as well as Eq. (32) the factorization of G has been fully accomplished as:

$$G_+(\lambda) \approx g_+(\lambda)G_{1+}(\lambda)G_{2+}(\lambda) \quad \text{and} \quad G_-(\lambda) \approx g_-(\lambda)G_{1-}(\lambda)G_{2-}(\lambda) \tag{40}$$

where:

$$g_\pm(\lambda) = \sqrt{2k_0\alpha}\left(\lambda \mp \sqrt{\epsilon_{r1}}\right) \tag{41}$$

3.3. Solution of the Wiener-Hopf Equation

Returning back to Eq. (12) and substituting the factorized functions yields:

$$\frac{R_+(\lambda)}{G_+(\lambda)} = G_-(\lambda)L_-(\lambda) - \tilde{j}_+^i(\lambda)G_-(\lambda) \tag{42}$$

The last term of Eq. (42) must be decomposed to "positive" and "negative" functions $S_\pm(\lambda)$. As explained in [9], this is essentially done by adding and subtracting the residue contribution at $\lambda = \sqrt{\epsilon_{r1}}$, and this is in accordance to [14, p. 94]:

$$\tilde{j}_+^i(\lambda) \cdot G_-(\lambda) = s_-(\lambda) + S_+(\lambda) = \tilde{j}_+^i(\lambda)\left[G_-(\lambda) - G_-(\lambda = \sqrt{\epsilon_{r1}})\right] + \tilde{j}_+^i(\lambda) \cdot G_-(\lambda = \sqrt{\epsilon_{r1}}) \tag{43}$$

The singularity $\lambda = +\sqrt{\epsilon_{r1}}$ is in the lower λ-plane as justified by considering the dielectric losses in ϵ_{r1} as:

$$\lambda = \sqrt{\epsilon_{r1}} = \left[\epsilon_{r1}'(1 - j\tan\delta)\right]^{\frac{1}{2}} = n_1' - jn_1'' \tag{44}$$

Hence, Eq. (43) indeed removes this singularity from the lower λ-half plane ensuring the analyticity of the "negative" term, while this pole is absorbed in the "positive" term as:

$$\frac{\tilde{R}_+(\lambda)}{G_+(\lambda)} + \tilde{j}_+^i(\lambda) \cdot G_-(\lambda = \sqrt{\epsilon_{r1}}) = G_-(\lambda)\tilde{L}_-(\lambda) - \tilde{j}_+^i(\lambda) \cdot \left[G_-(\lambda) - G_-(\lambda = \sqrt{\epsilon_{r1}})\right] = \tilde{P}(\lambda) \tag{45}$$

Notably, the assumption in Eq. (44) is valid in the frequency bands $\Omega < R$ and $\Omega > \sqrt{R^2 + 1}$ where ϵ_{r1} is positive, (Figs. 5–6 below). Outside this range ϵ_{r1} becomes negative, while plasma permeability remains positive, thus the wave ceases to propagate according to Eq. (12). Namely, even the incident

wave becomes evanescent. According to Liouville's theorem, the "positive" and "negative" terms as Eq. (45) can be equal only within the common analyticity strip $-\alpha_+ = \tau_- \leq \text{Im}(\lambda) \leq \alpha_- = \tau_+$ illustrated in Fig. 2. Hence $\tilde{P}(\lambda)$ must be an entire function within that strip equal to a constant or having a polynomial behavior. This is in turn defined by the edge condition along $z = 0$. An asymptotic approximation of the involved functions $(\lim f(z) \text{ for } (z \to 0))$ indicates that $\tilde{j}_+^i(\lambda)$ varies as λ^{-1} and $G_-(\lambda), G_+(\lambda) \propto \lambda^{\frac{1}{2}}$. Recall that field components H_y, E_x parallel to the edge at $z = 0$ tend to zero as $\propto z^{+\frac{1}{2}}$ as $z \to 0$, while those normal to the metallic edge (E_x, E_z) tend to infinity as $\propto z^{-\frac{1}{2}}$. Thus, the terms $\tilde{S}_+(\lambda)$ and $\tilde{S}_-(\lambda)$ are proportional to λ^{-1} and $\lambda^{-\frac{1}{2}}$ as $z \to 0$. Overall, all terms in Eq. (45) tend to zero as $|\lambda| \Rightarrow \infty$ corresponding to the edge condition $z \to 0$. This means that the entire function $\tilde{P}(\lambda)$ is identically zero, leading to the solution in the transformed domain:

$$\tilde{R}_+(\lambda) = -\tilde{j}_+^i(\lambda)\, G_+(\lambda)\, G_-(\lambda = \sqrt{\epsilon_{r1}}) \tag{46a}$$

and

$$\tilde{L}_-(\lambda) = \frac{\tilde{S}_-(\lambda)}{G_-(\lambda)} = \tilde{j}_+^i(\lambda)\left[1 - \frac{G_-(\lambda = \sqrt{\epsilon_{r1}})}{G_-(\lambda)}\right] \tag{46b}$$

The spectral functions $\tilde{R}_+(\lambda)$ and $\tilde{L}_-(\lambda)$ can be substituted back to the field expressions to yield their spectral representation. However, the major difficulty is then encountered within the inverse Fourier transform, necessary to extract the true field in the spatial domain. This task is elaborated in the next section. Besides the field components, it is interesting to estimate the total current density $J_{sz}(z < 0)$ induced on the truncated conductor, $(x = \alpha, z < 0)$. This is readily given in Eq. (23) of our previous work [9], which can be reformulated in the spectral domain as:

$$\tilde{j}_-^t(\lambda) = Q(\lambda)\,\tilde{R}_+(\lambda) + \tilde{j}_-^i(\lambda) \tag{47}$$

The second term in the right-hand side is the "negative" spectral function representing the Fourier transform of the current induced on the truncated conductor by the incident field, which is given in Eq. (24) of [9] as:

$$\tilde{j}_-^i(\lambda) = j\frac{1}{2\pi\left(\lambda + \sqrt{\epsilon_{r1}}\right)} \cdot \exp\left(k_0\epsilon_{r2}\alpha/\sqrt{\epsilon_{r1}}\right) \tag{48}$$

It is now obvious that the term $Q(\lambda)\tilde{R}_+(\lambda)$ represents the induced current density due to the scattered field, (i.e., $\tilde{j}_-^s(\lambda)$). The kernel $Q(\lambda)$ is already factorized as $Q(\lambda) = \frac{1}{G(\lambda)} = \frac{1}{G_+(\lambda)G_-(\lambda)}$. Thus, substituting $\tilde{R}_+(\lambda)$ from Eq. (46a) yields the induced spectral total current density:

$$\tilde{j}_-^t(\lambda) = -\tilde{j}_+^i(\lambda)\left[1 - \frac{G_-(\lambda = \sqrt{\epsilon_{r1}})}{G_-(\lambda)}\right] + \tilde{j}_-^i(\lambda) \tag{49}$$

Notably Eq. (49) resembles $\tilde{L}_-(\lambda)$ in Eq. (46b), but with a major difference that Eq. (46b) involves only the fictitious current $\tilde{j}_+^i(\lambda)$ assumed at the plasma-air interface.

For the evaluation of the magnetic field within the plasma region, $(-\alpha \leq x \leq \alpha)$, the Wiener-Hopf solution is substituted back in Eq. (5a) through the coefficients of Eqs. (9)–(10) following the inverse Fourier transform of Eq. (2). There are two important observations within this procedure. First, the coefficients $B_p(\lambda)$ and $C_p(\lambda)$ include the product $u_0 A_p(\lambda) = R_+(\lambda)$, thus the branch-cut $\text{Im}(u_0) = 0$ disappears, or there is not any contribution from the space wave (continuous spectrum) as expected. The second point refers to the assumed fictitious TEM wave propagation, unattenuated beyond the edge $z = 0$ toward $z > 0$. Thus, its field must be subtracted from the total field by its corresponding pole contribution at $\lambda = \sqrt{\epsilon_{r1}}$ as noted in Eq. (13). This means that the assumed fictitious current $J_+(z > 0)$ at the plasma-air interface generates a virtual wave equal to the residue of Eq. (5a) at $\lambda = \sqrt{\epsilon_{r1}}$. The total induced current at the truncated conductor $J_{sz}^t(z < 0, x = \alpha)$ is evaluated from the inverse Fourier transform of Eq. (49) by integrating along C_- of Fig. 2 closed in the upper λ-half plane. For radiation purposes, it should be ensured that J_{sz}^t should be identically at the plasma-air interface $x = \alpha$, $z > 0$. Indeed, functions $G_-(\lambda)$ and $\tilde{j}_-^i(\lambda)$ are analytical in the lower λ-half plane when for $z > 0$ the contour C_+ (Fig. 2) is followed. However, Eq. (49) involves also the fictitious spectral current $\tilde{j}_+^i(\lambda)$ which has
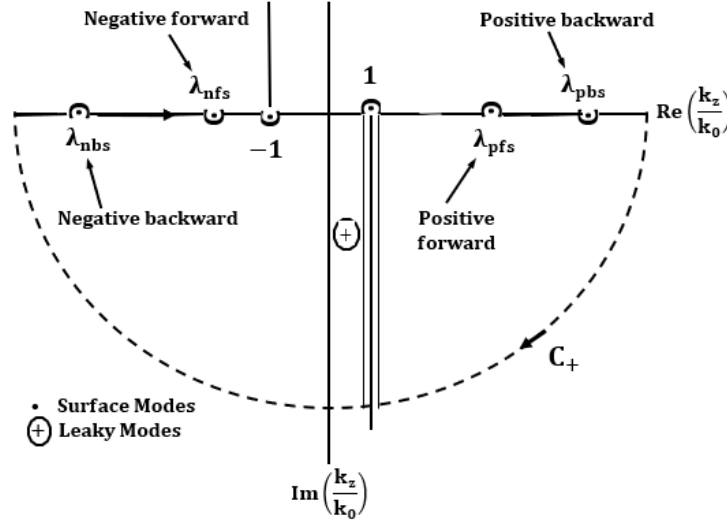
Figure 3. Poles and the integration path for the inversion of open geometry for $z > 0$. Positive-negative forward-backward modes are indicated.

a pole at $\lambda = \sqrt{\epsilon_{r1}}$ according to Eq. (14), thus in the lower λ-half plane. This means that the inversion of Eq. (49) will indeed yield the assumed fictitious current at $x = \alpha$, $z > 0$ as expected.

The path of integration along with the involved singularities for each one of the above cases is illustrated in Fig. 3. These singularities include the branch-cuts (for the air region fields), the TEM wave pole at $\lambda = -\sqrt{\epsilon_{r1}}$ for the parallel plane region, the fictitious pole at $\lambda = +\sqrt{\epsilon_{r1}}$, the forward surface and leaky wave poles at $\lambda = a_{nfs}$ and $\lambda = a_{nfl}$, as well as the backward surface and leaky wave poles at $\lambda = a_{nbs}$ and $\lambda = a_{nbl}$.

Regarding the TEM wave reflection coefficient Γ_{TEM} is estimated from the residue contribution of the scattered magnetic field H_y^s of Eq. (5a) in the parallel plane region, $(-\alpha \leq x \leq \alpha, z < 0)$ at $\lambda = -\sqrt{\epsilon_{r1}}$. This is depicted below according to [9] as:

$$H_y^r = \Gamma_{\text{TEM}} \exp\left(-\frac{k_0 \epsilon_{r2} x}{\sqrt{\epsilon_{r1}}} + jk_0\sqrt{\epsilon_{r1}}z\right) \quad \text{and} \quad E_x^r = -\frac{\zeta_0}{\sqrt{\epsilon_{r1}}} \cdot H_y^r \tag{50a}$$

with

$$\Gamma_{\text{TEM}} = \frac{H_{y(\text{ref})}\Big|_{\lambda = -\sqrt{\epsilon_{r1}},\, z=0,\, x=\alpha}}{H_{y(\text{inc})}^{\text{TEM}}\Big|_{z=0,\, x=\alpha}} = \frac{2\pi j\, Res\left(H_{y(\text{ref})}(\lambda), -\sqrt{\epsilon_{r1}}\right)\Big|_{z=0,\, x=\alpha}}{H_{y(\text{inc})}^{\text{TEM}}\Big|_{z=0,\, x=\alpha}}$$

$$= -\frac{G_+\left(\lambda = -\sqrt{\epsilon_{r1}}\right) G_-\left(\lambda = \sqrt{\epsilon_{r1}}\right)}{8\epsilon_{r1}} \cdot \left[-2\epsilon_{r2}\sqrt{\epsilon_{r1}} + \epsilon_{r1}\sqrt{\epsilon_{r1} - \epsilon_{r\text{eff}}}\,\coth\left(k_0\sqrt{\epsilon_{r1} - \epsilon_{r\text{eff}}}\,\alpha\right)\right.$$

$$\left. +\epsilon_{r1}\sqrt{\epsilon_{r1} - \epsilon_{r\text{eff}}}\,\tanh\left(k_0\sqrt{\epsilon_{r1} - \epsilon_{r\text{eff}}}\,\alpha\right)\right] \tag{50b}$$

The far field especially in the case of unidirectional modes is elaborated in the next section.

3.4. Field Expressions in the Spatial Domain

The field expressions in the spectral domain can be readily obtained by substituting the Wiener-Hopf solutions $\tilde{R}_+(\lambda)$ and $\tilde{L}_-(\lambda)$ back to Eqs. (5)–(10) for the plasma and air regions. However, the useful quantities are the true field components and the induced current in the spatial domain. For this purpose,

the inverse Fourier transform of Eq. (2) must be employed remembering that in order for the field to vanish at infinity, $(z \to \pm\infty)$, the integration path must be closed in the lower λ-half plane to recover the function for $z > 0$ domain, i.e., following C_+ in Fig. 2. Likewise, for the negative $z < 0$ domain the integration must be closed in the upper λ-half domain along C_- in Fig. 2. Starting from the magnetic field in the air region, $(x \geq \alpha)$, Eqs. (2) and (7a) yield: The scattered field is determined by solving the inverse Fourier transform integral of Eqs. (2a)–(b). Using Eqs. (5a), (6), (7a), (9), (10), (11), and (46a), the solution referred to modal poles of the field problem results:

- air region, $(x \geq \alpha)$:

$$H_y^s = -\int_{C_\pm} \frac{\tilde{R}_+ (\lambda)}{u_0} e^{-k_0 u_0 (x-\alpha)} e^{-jk_0 \lambda z} d\lambda, \quad C_+ \text{ for } z \geq 0, \; C_- \text{ for } z < 0 \tag{51}$$

or in an alternative form setting Eq. (46a) to Eq. (51):

$$H_y^s = -\frac{je^{\frac{k_0 \epsilon_{r2} \alpha}{\sqrt{\epsilon_{r1}}}} G_- \left(\lambda = \sqrt{\epsilon_{r1}}\right)}{2\pi} \int_{C_\pm} \frac{G_+ (\lambda) e^{-k_0 u_0 (x-\alpha)} e^{-jk_0 \lambda z}}{u_0 \left(\lambda - \sqrt{\epsilon_{r1}}\right)} \, d\lambda, \quad C_+ \text{ for } z \geq 0, \; C_- \text{ for } z < 0 \tag{52}$$

There is an important observation regarding Eq. (51). The positive function $\tilde{R}_+(\lambda)$ is analytic in the upper λ-half plane where C_- is closed for $z < 0$. Hence, the integral in Eq. (51) does not enclose any pole singularities for $z < 0$, and the scattered waves propagating toward $z < 0$ are solely due to the branch-cut integral $u_0 = \sqrt{\lambda^2 - 1}$ also included in Eq. (51). Namely, the field toward negative z in air is composed only from the space wave or continuous spectrum, without any surface or leaky wave contribution. Notably, this observation may not be general, but it may be valid only for the normally incident TEM wave considered herein. The same conclusion applies for the transverse electric field E_x^s component according to Eq. (8). On the contrary, the axial scattered electric field E_z^s seems to exist only for $z > 0$ and being identically zero for the whole $z < 0$ half domain, as Eqs. (8) and (2) results to:

$$E_z^s = \int_{C_\pm} j\zeta_0 \tilde{R}_+ (\lambda) e^{-k_0 u_0 (x-\alpha)} e^{-jk_0 \lambda z} d\lambda, \quad C_+ \text{ for } z \geq 0, \; C_- \text{ for } z < 0 \tag{53}$$

Notably, the branch point $u_0 = 0$ and the branch-cut $\text{Im}(u_0) = 0$ are absent from the integrand in Eq. (53). This result is also verified by Noble [17, p. 107], where the radiation from an open-ended parallel plane waveguide is studied.

- plasma region, $(-\alpha \leq x \leq \alpha)$:

$$\begin{aligned} H_y^s &= \frac{je^{\frac{E^{k_0 \epsilon_{r2} \alpha}}{\sqrt{\epsilon_{r1}}}}}{4\pi} G_- \left(\lambda = \sqrt{\epsilon_{r1}}\right) \left\{ \int_{C_\pm} \left[\frac{\lambda \epsilon_{r2}}{\cosh (k_0 u_p \alpha)} + \frac{\epsilon_{r1} u_p}{\sinh (k_0 u_p \alpha)} \right] \right. \\ &\quad \cdot \frac{\cosh (k_0 u_p x)}{(\lambda^2 - \epsilon_{r1}) \left(\lambda - \sqrt{\epsilon_{r1}}\right)} G_+ (\lambda) e^{-jk_0 \lambda z} d\lambda + \int_{C_\pm} \left[\frac{\epsilon_{r1} u_p}{\cosh (k_0 u_p \alpha)} + \frac{\lambda \epsilon_{r2}}{\sinh (k_0 u_p \alpha)} \right] \\ &\quad \left. \frac{\sinh (k_0 u_p x)}{(\lambda^2 - \epsilon_{r1}) \left(\lambda - \sqrt{\epsilon_{r1}}\right)} G_+ (\lambda) e^{-jk_0 \lambda z} d\lambda \right\}, \quad C_+ \text{ for } z \geq 0, \; C_- \text{ for } z < 0 \tag{54} \end{aligned}$$

Expression (54) results from setting Eqs. (46a), (15), (9), (10) to (5a), giving the magnetic field expression inside the plasma slab region for $-\alpha < x < \alpha$, $z > 0$.

Poles involved in the field expressions of Eqs. (52) and (54) can be either refer to those on the lower or upper complex half domain represented in Fig. 2, as Eqs. (52), (54) dictate, in order to evaluate field for $z > 0$ or $z < 0$ sub-spaces respectively. Surface wave poles are on the real axis (Fig. 3), and the integration contour has to be indented in the vicinity of these poles, in order the radiation condition to be satisfied.

3.5. Far Field Calculation

Whenever one attempts to estimate the radiation from a structure, it is expected that the radial field components will vanish. Thus, in general the field components are transformed to a spherical coordinate system when a three-dimensional structure is examined. But herein the structure under study is a two dimensional one, and it could be considered as a radiating aperture at $-\alpha < x < \alpha$, $z = 0$ extending to infinity along the $\hat{y}$ direction. Hence, a transformation from cartesian (x, y, z) to cylindrical $(\rho, \theta, \hat{y})$ may be sought as:

$$x - \alpha = \rho \sin \theta, \;\; z = \rho \cos \theta; \;\; \rho = \sqrt{(x - \alpha)^2 + z^2}, \;\; \theta = \tan^{-1}\left[(x - \alpha)/z\right] \tag{55a}$$

With this transformation a vector $\vec{A} = \hat{x} A_x + \hat{y} A_y + \hat{z} A_z = \hat{\rho} A_\rho + \hat{\theta} A_\theta + \hat{y} A_y$, and the relations read:

$$A_\rho = A_z \cos \theta + A_x \sin \theta, \quad A_\theta = -A_z \sin \theta + A_x \cos \theta, \quad A_y = A_y \tag{55b}$$

As depicted in Eqs. (7) and (8), the scattered field in the air regions exhibits the components, (H_y^s, E_x^s, E_z^s), which after the transformation in Eq. (53) will turn to $H_y^s, E_\rho^s, E_\theta^s$. Thus, the magnetic field is retained as an H_y^s while the radial electric field E_ρ^s is expected to vanish in the far field approximation, $(E_\rho^s \to 0$ when $\rho \to \infty)$. Thus, a far field of $H_y^s(\rho, \theta)$ and $E_\theta(\rho, \theta)$ is sought through the transformation in Eq. (55b) and $\rho \gg$. Since a plane wave is expected in the far field, we may restrict the calculations to $H_y^s(\rho, \theta)$, and the electric field can be estimated through the characteristic impedance as $E_\theta^s = \zeta_0 H_y^s$. As a first step, the transformation in Eq. (55a) is utilized in Eq. (51) to yield:

$$H_y^s = \int_{C_\pm} \frac{\tilde{R}_+(\lambda)}{u_0} e^{-k_0 u_0 \rho \sin \theta} e^{-j k_0 \lambda \rho \cos \theta} d\lambda, \quad C_+ \text{ for } z \geq 0, \;\; C_- \text{ for } z < 0 \tag{56}$$

Asymptotic evaluation of integrals as the above of Eq. (56) is well established through the steepest descent approximation, e.g., Felsen & Marcuvitz [19, Ch. 3] is employed in order to remove the branch-cut, from the normalized wavenumber $\lambda = \frac{\beta_z}{k_0} - j\frac{\alpha_z}{k_0}$ to a complex domain $\varphi = \varphi_r + j\varphi_i$ as:

$$\lambda = \cos \varphi, \quad u_0 = \sqrt{\lambda^2 - 1} = j\sqrt{1 - \lambda^2} = j \sin \varphi \quad \text{and} \quad d\lambda = -\sin \varphi \, d\varphi \tag{57}$$

Following Eq. (57), the original integration path C is transformed to the steepest descent path SDP, which is different for each observation angle θ. As usual the SDP crosses the original path across φ_r axis at the saddle point $\varphi_r = \theta$. Since θ is defined from $\theta = 0$ to $\theta = \pi$, two corresponding SDP paths are depicted as LSDP and USDP, which are illustrated in Fig. 13. The SDP and the original path are connected at the infinity, and the singularities enclosed-captured are the same enclosed in the original path $C_\pm$ of Fig. 2. Thus, as angle θ scans from 0 to π all pole singularities included between LSDP and USDP contribute to the radiation at some angle θ. The contribution of these poles to the integral is accounted through their residues. The contribution along SDP is approximated by the standard saddle point approximation [17], to yield the space wave or continuous wave spectrum contribution, which for Eq. (56) reads:

$$H_y = \sqrt{\frac{k_0}{2\pi\rho}} \, e^{\frac{k_0 \epsilon_{r2} \alpha}{\sqrt{\epsilon_{r1}}}} \frac{1}{\left(\cos \theta - \sqrt{\epsilon_{r1}}\right)} G_+(\cos \theta) \, G_-(\lambda = \sqrt{\epsilon_{r1}}) \, e^{-j k_0 \rho + j \frac{\pi}{4}} \tag{58}$$

or similarly

$$H_y = k_0 \sqrt{\frac{\alpha}{\pi\rho}} \, e^{\frac{k_0 \epsilon_{r2} \alpha}{\sqrt{\epsilon_{r1}}}} G_{1+}(\cos \theta) \, G_{2+}(\cos \theta) \, G_-(\lambda = \sqrt{\epsilon_{r1}}) \, e^{-j k_0 \rho + j \frac{\pi}{4}} \tag{59}$$

The above complex modes contribute to the field as it is stated by Felsen for $e^{+j\omega t}$ dependence [19, Ch. 5], since they are positioned (Fig. 12), in the #4 quadrant, $(\text{Re}(\lambda) = \beta_z/k_0 > 0$ and $\text{Im}(\lambda) = -\alpha_z/k_0 < 0)$. A careful examination of Table 3 and Figs. 12–13, as well as the characteristic equation $Q(\lambda) = 0$, reveals that for $k_0 2\alpha = 0.3$ and $\Omega = 0.15$, the first surface wave mode is always excited, but it is "captured" by the SDP at the observation angle, (saddle point) $\theta = \theta_{1s} = 12°$. Likewise, the higher order surface modes are captured at: $\theta = \theta_{ns} = 63°$. In a similar manner, the first leaky mode $(\beta_z/k_0 < 1)$ is captured at: $\theta = \theta_{1l} = 0.2°$.

4. NUMERICAL RESULTS

4.1. Excited Modes

The analytical study presented in the previous sections can be exploited in a plethora of magnetized solid state plasma substrates. A general approach adopted by Seshadri et al. [10] considers an arbitrary normalized substrate thickness $(k_0 2\alpha)$, but herein we focus on electrically thin structures. For this problem to be meaningful the existence-propagation of the incident TEM wave in the parallel plane waveguide must be ensured. From Eq. (12) its propagation in the z-direction requires ϵ_{r1} to be positive, since its magnetic permeability is also positive $(\mu = \mu_0)$. Furthermore, the properties of the waves excited in the grounded substrate regions $(z > 0)$ are affected by the plasma effective dielectric constant ϵ_{reff} as denoted by Eq. (5b), which will in turn identify the surface and leaky modes. Hence, the elements of the permittivity tensor ϵ_{r1}, ϵ_{r2}, ϵ_{r3}, and ϵ_{reff} given in Eq. (3) versus the normalized frequency $\Omega = \omega/\omega_p$ are illustrated in Figs. 5–6, which tend to infinity at $\Omega = R$ or zero.

    An insight into the scattering phenomena occurring when the extra-ordinary TEM wave is incident at the aperture (at $z = 0$) defined by the upper conductor $(x = \alpha, z \leq 0)$ is illustrated in Fig. 4. From a qualitative point of view, rays are emanating from the aperture toward all possible directions both towards the positive $z > 0$ area as well as toward the parallel plane area $z < 0$. The latter constitute waves guided in a parallel plane waveguide, from which only the TEM wave exhibits constructive interference (propagation) due to the small thickness of the plasma layer, while all higher order modes

Table 3. Characteristics of modes regarding normalized propagation constant and its transform to complex angle domain.

$k_0 2\alpha = 0.3,\ R = 0.5$		$\lambda = \beta_z/k_0 - j\alpha_z/k_0$		$\varphi = \varphi_r + j\varphi_i$	
		β_z/k_0	α_z/k_0	φ_r (degrees)	φ_i (degrees)
Proper Surface Modes		1.026	0	0	-13.04
		2.4699	0	0	-85.14
		-1.00405	0	180	5.15
Improper Modes	Leaky	0.902	11.97	85.71	182.21
	Improper Complex	1.107	21.743	87.086	216.249
		1.156	31.956	87.929	238.259
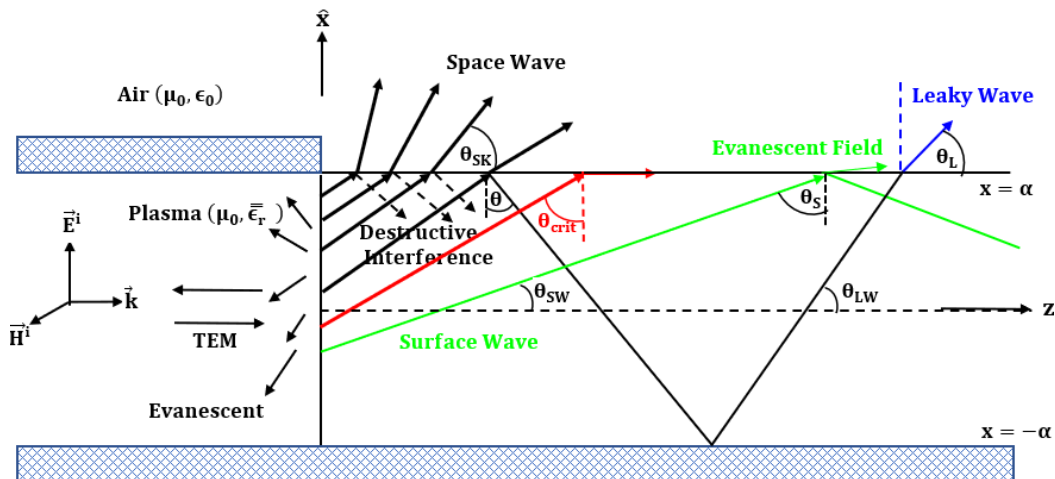
Figure 4. Qualitative insight into the scattered waves at the aperture $(z = 0)$ defined by the truncated conductor (at $z \leq 0$, $x = \alpha$): sky or space waves, leaky waves and surface waves.
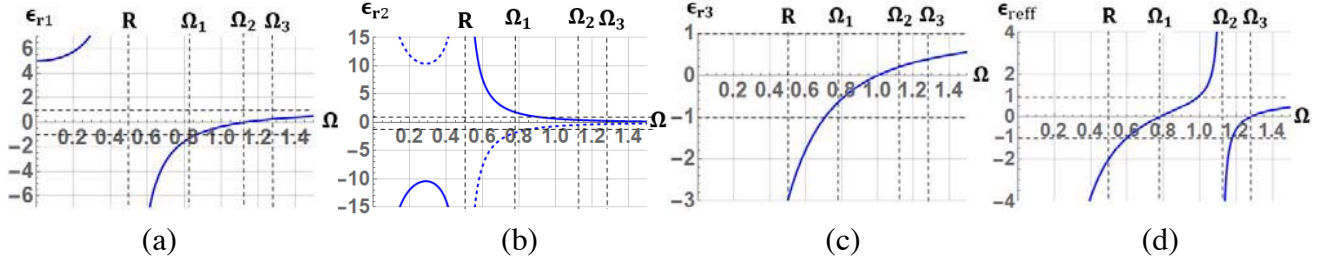
Figure 5. Plasma tensor entries (a) ϵ_{r1}, (b) ϵ_{r2}, (c) ϵ_{R3} and (d) ϵ_{reff} as a function of the normalized frequency Ω for $R = 0.5 < \Omega_1$ ($R < 1$). Dashed blue lines denote $H_0\hat{y}$, ($R = -0.5$), bias, whereas continuous blue lines $-H_0\hat{y}$ bias, ($R = 0.5$) [10, p. 531].
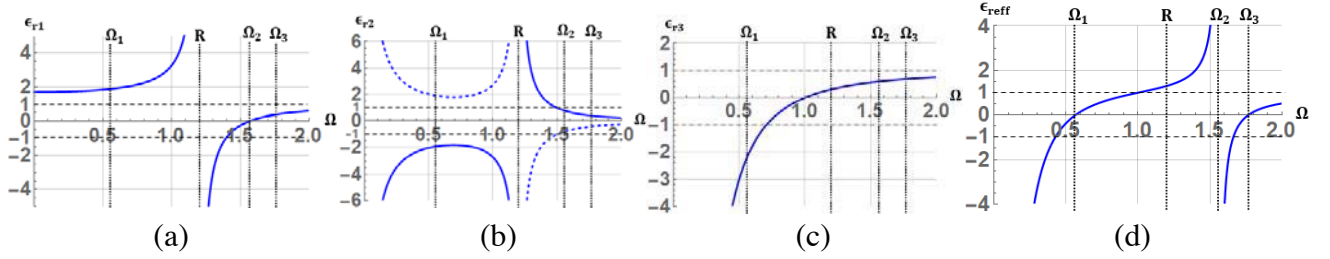
Figure 6. Plasma tensor entries (a) ϵ_{r1}, (b) ϵ_{r2}, (c) ϵ_{r3} and (d) ϵ_{reff} as a function of the normalized frequency Ω for $R = 1.2 > \Omega_1$ ($R > 1$). Dashed blue lines denote $+H_0\hat{y}$ bias, ($R = -1.2$), whereas continuous blue lines $-H_0\hat{y}$ bias, ($R = 1.2$) [10, p. 531].

are evanescent. Regarding the rays toward positive z, emanating at angles $\theta < \theta_{\mathrm{crit}}$ these are diffracted at the plasma air interface, and their main energy part propagates away towards the air region as space or sky wave. Their propagation within the plasma layer is affected by its characteristics, but in the air region they propagate at free space-air wavenumber k_0. Notably, their axial propagation constant $\beta_z = k_0 \sin \theta_S$ takes continuously all values $0 \leq \beta_z \leq k_0$, thus their contribution must be accounted for via integration (branch-cut integral). Most of the corresponding reflected waves undergo destructive interference, since they do not fulfill the guided wave conditions defined by the grounded plasma layer characteristic equation $Q(\lambda) = 0$ as in Equation (16). However, some specific rays (possibly only one) reflected at $\theta < \theta_{\mathrm{crit}}$ with $\beta_z < k_0$ may fulfill Eq. (16) exhibiting constructive interference or mode guidance withing the plasma layer, and these constitute the leaky waves. These undergo multiple diffractions at the plasma air interface, and at each one a significant amount of their energy leaks away toward the air region ($x > \alpha$) at an angle θ_L (Fig. 4). Their important difference from the sky wave radiation is that their axial propagation constant is complex, and it is identical within the plasma and the air region, as a result of the phase-matching condition at $x = \alpha$ interface. Hence, the nature of leaky waves and their capability to leak radiate energy is governed by their effective dielectric constant defined as $\epsilon_{reff}^{\mathrm{LW}} = (\beta_z/k_0)^2 = \mathrm{Re}(\lambda)^2 = \lambda_r^2$, also $\beta_z^{\mathrm{LW}} = k_{\mathrm{plasma}} \cos \theta_{\mathrm{LW}}$. When $\epsilon_{reff}^{\mathrm{LW}}$ becomes negative, these waves cannot propagate, nor they can radiate energy. Rays emanating at angles greater than the critical ($\theta_S \geq \theta_{\mathrm{crit}}$), they undergo "total" reflection at the interface $x = \alpha$ (explicitly, their amplitude is exponentially decreased in the air region, evanescent), and most of them exhibit destructive interference in the plasma region. These may be interpreted as high order evanescent waves of the grounded plasma slab. But again, some of them fulfill the characteristic Equation (16) becoming propagating surface waves. Their axial propagation ($\beta_z^{\mathrm{SW}} = k_{\mathrm{plasma}} \cos \theta_{\mathrm{SW}}$) is greater than free space wave number ($\beta_z^{\mathrm{SW}} \geq k_0$) and is identical in the air and plasma regions due to phase matching at the interface $x = \alpha$. In the ordinary dielectric substrate case, their transverse phase constant is zero ($\beta_x^{\mathrm{SW}} = \mathrm{Im}(u_0) = 0$), and they are exponentially vanishing away from $x = \alpha$ as $e^{-k_0 u_0 x}$ (where $u_0 = u_{0r} > 0$ and real). However, in the grounded plasma case u_0 becomes complex, thus yielding to propagation or energy leakage away from $x = \alpha$ toward the air region. But, in order for them

Table 4. Summary of properties in different frequency ranges for $R < 1$ [10, 12].

Ω	ϵ_{r1}	ϵ_{r2}	ϵ_{reff}	Lowest Order Surface Wave
$0 < \Omega < R$	+	−	−	Lower Conductor
$R < \Omega < \Omega_1$	−	+	−	Evanescent
$\Omega_1 < \Omega < \Omega_2$	−	+	+	Evanescent
$\Omega_2 < \Omega < \Omega_3$	+	+	−	Upper Conductor
$\Omega_3 < \Omega < \infty$	+	+	+	Upper Conductor

Table 5. Summary of properties in different frequency ranges for $R > 1$ [10, 12].

Ω	ϵ_{r1}	ϵ_{r2}	ϵ_{reff}	Lowest Order Surface Wave
$0 < \Omega < \Omega_1$	+	−	−	Lower Conductor
$\Omega_1 < \Omega < R$	+	−	+	Lower Conductor
$R < \Omega < \Omega_2$	−	+	+	Evanescent
$\Omega_2 < \Omega < \Omega_3$	+	+	−	Upper Conductor
$\Omega_3 < \Omega < \infty$	+	+	+	Upper Conductor

to propagate their effective dielectric constant must be positive $\epsilon_{reff}^{\mathrm{SW}} = (\beta_z^{\mathrm{SW}}/k_0)^2 = \lambda_r^2 > 0$, (where $\lambda_r = \mathrm{Re}(\lambda)$). Overall, in the plasma case herein we expected radiation from sky wave, leaky waves, but also from complex surface waves. Evidence for these characteristics is also provided by Seshadri et al. [10] as well as Felsen [19, p. 869]. Explicitly, Seshadri [10] points out that space wave can provide radiation on every $\epsilon_{reff} = \epsilon_{rq}/\epsilon_{r1}$ range defined in Eq. (3). It is also stated by Felsen [19, p. 869] that "real energy may be extracted by the surface waves", even in the cases of an outer anisotropic region. In the present case, complex surface modes provide radiation, especially in low frequency zones, as they radiate "practically unattenuated" (as stated by Seshadri [10]), in the air region, depended on their residue strength. This happens, since their purely "real" propagation constant λ tends to unity [10]. Leaky modes', $(\beta_z^{\mathrm{LW}}/k_0 < 1)$, radiation mechanism depends only on their position on steepest descent, (SDP), plane [24, Part II, Appendix of Ch. 21].

The defined frequency regions for the two cases when $R > 1$ or $R < 1$ are depicted in Tables 4 and 5, respectively. Of particular importance is the range $\Omega \to 0$ where unidirectional waves are observed [10, 11]. Observing Figs. 5–6, it is obvious that there are frequency bands where the entries of the permittivity tensor, and ϵ_{reff} become negative as:

$$0 < \epsilon_{reff} < 1 \text{ for } \Omega_1 < \Omega < 1 \text{ and } \Omega_3 < \Omega < +\infty \tag{60a}$$

$$1 < \epsilon_{reff} < +\infty \text{ for } 1 < \Omega < \Omega_2 \tag{60b}$$

$$-\infty < \epsilon_{reff} < 1 \text{ for } < \Omega < \Omega_1 \text{ and } \Omega_2 < \Omega < \Omega_3 \tag{60c}$$

where

$$\Omega_1 = \frac{-R + \sqrt{R^2 + 4}}{2}, \ \Omega_2 = \sqrt{R^2 + 1}, \ \Omega_3 = \frac{R + \sqrt{R^2 + 4}}{2} \tag{60d}$$

Older works on magnetized plasma, e.g., [10, 12] examined only the effects of surface waves; however nowadays it is necessary to investigate leaky waves as well. Since the magnetized plasma tensor is complicated, it is a good idea to utilize the case of ordinary dielectric substrate as a guide to identify the condition for a leaky wave to exist. It is well understood, in dielectrics, that surface waves become leaky for frequencies below their cut-off, (turn-on). The first surface wave has zero cut-off, thus for a leaky wave to exist the substrate must support at least the second (or any higher) surface wave. The condition for the excitation of the second surface wave is, e.g., Pozar [25, p. 144]:

$$k_0 2\alpha \cdot \sqrt{\epsilon_{reff} - 1} \geq \pi \Rightarrow k_0 2\alpha \cdot \sqrt{\epsilon_{reff} - 1} \geq \pi \tag{61}$$

The supported waves are classified by Seshadri and Pickard [10], into four cases. These are also elaborated in our previous works [13], using the present symbolism and discriminating the leaky wave regimes. They are further identified as "Type-1" and "Type-2", and a summary of their characterization is depicted in Table 6 based on λ. Notably, all cases are solutions of the characteristic Equation (16), $Q(\lambda) = 0$ for different parameters (Table 6).

Table 6. Classification of modes, supported by a grounded magnetized plasma slab [10, 13].

	Case	u_0	u_p	Characterization
1	$\lambda^2 \leq 1, \lambda^2 \leq \epsilon_{reff}$	$j\lvert u_0\rvert$	$j\lvert u_p\rvert$	Improper Complex ($\beta_z/k_0 > 1$) or Leaky ($\beta_z/k_0 < 1$)
2	$\lambda^2 \leq 1, \lambda^2 \geq \epsilon_{reff}$	$j\lvert u_0\rvert$	$\lvert u_p\rvert$	Improper Complex ($\beta_z/k_0 > 1$) or Leaky ($\beta_z/k_0 < 1$)
3	$\lambda^2 \geq 1, \lambda^2 \leq \epsilon_{reff}$	$\lvert u_0\rvert$	$j\lvert u_p\rvert$	Proper Surface ($\beta_z/k_0 > 1$)
4	$\lambda^2 \geq 1, \lambda^2 \geq \epsilon_{reff}$	$\lvert u_0\rvert$	$\lvert u_p\rvert$	Proper Surface ($\beta_z/k_0 > 1$)

As noted in [10] and further in [13], there are no real roots (poles) in cases-1 and -2. These complex roots represent "improper modes", which under certain condition may yield useful "leaky waves". On the contrary, cases-3 and -4 with $\lvert\lambda\rvert = \lvert\beta_z/k_0\rvert \geq 1$ support two types of surface waves. Type-1 surface waves exist in the range $1 < \Omega < \sqrt{1 + R^2}$ exhibiting a cut-off (turn-on) frequency at $\Omega > 1$, while they are always forward (by means of $u_p \cdot u_g > 0$). Obviously, $\lambda_r^2 > 0$ (Fig. 7) in all the examining frequency range. The same observation occurs later for leaky waves, also. So, term ϵ_{r1} is needed to be positive (in order incident TEM wave to propagate), for the modes to be excited. Thus, they propagate inside the structure. When examining their dispersion curves these are expected to become leaky waves at frequencies below their turn-on. Type-2 surface waves that exist in the range $0 < \Omega < \sqrt{1 + R^2}$ do not have a low frequency cut-off and may present sub-ranges with "backward" behavior (by means of $u_p \cdot u_g < 0$). For ordinary dielectric substrates $\epsilon_{reff} > 1$ their zero cut-off would prohibit them from transforming to leaky waves. However, for the magnetized plasma the negative permittivity entries and the possibility of $\epsilon_{reff} < 1$ generates leaky and improper surface waves sub-zones. Certain Type-2 surface waves present a unidirectional behavior propagating towards positive $\hat{z}$ and concentrated along the plasma-air interface ($x = \alpha$) or propagating towards negative $\hat{z}$ direction and concentrated along the bottom grounded metallic screen ($x = -\alpha$) [10]. This is justified by Eq. (12) which yields a dependence:

$$\text{Unidirectional forward surface wave}: \quad H_y \propto e^{\frac{k_0 \epsilon_{r2}(x-\alpha)}{\sqrt{\epsilon_{r1}}}} \cdot e^{-jk_0\sqrt{\epsilon_{r1}}\cdot z} \tag{62a}$$

for $0 < \Omega < \sqrt{1 + R^2}$ it is $\epsilon_{r2} < 0$ and $\epsilon_{r1} > 0$ but as $\Omega \to 0$, $\epsilon_{r2} \to -\infty$ restricting the field around $x = \alpha$ interface.

On the contrary, waves in the plasma region propagating towards negative z behave as Eq. (62b), thus concentrating around $x = -\alpha$ at very low frequencies $\Omega \to 0$.

$$\text{Unidirectional reverse surface wave}: \quad H_y \propto e^{\frac{-k_0 \epsilon_{r2}(x+\alpha)}{\sqrt{\epsilon_{r1}}}} \cdot e^{+jk_0\sqrt{\epsilon_{r1}}\cdot z} \tag{62b}$$

The dispersion curves of the two types of surface waves (Type-1, Type-2) are illustrated in Fig. 7(a) for an electrically thin substrate in the range of $k_0 2\alpha = 0.1$ to 1 versus normalized frequency Ω, while the gyromagnetic frequency is varied in Figs. 7(b), (c).

For the classical proper surface waves (Fig. 7), where $\lambda = \beta_z/k_0 > 1$, the transverse propagation constant $u_0 = \sqrt{\lambda^2 - 1} = u_{0r}$ is purely real and plotted in Fig. 8(a) as a function of frequency for the indicative substrate thickness $k_0 2\alpha = 0.1$. Next in Fig. 8(b), the phase constant $\lambda = \lambda_R = \beta_z/k_0$ for surface modes is examined versus the normalized frequency Ω, in order to reveal the ranges where forward or backward propagation occurs.

As explained in the literature [24, Part II], modes with purely real wavenumbers are named surface modes, either proper, or improper. However, for plasma loaded structures most of the discrete modal spectrum consists of complex waves [23, 24, 26, 27]. Recalling the well-known properties of "pole contributions [19, Ch. 5], only modes positioned on #2, or #4 quadrants (Fig. 11) contribute to the field. Special attention should be given on complex poles of #4 quadrant, which consist of pole-solutions
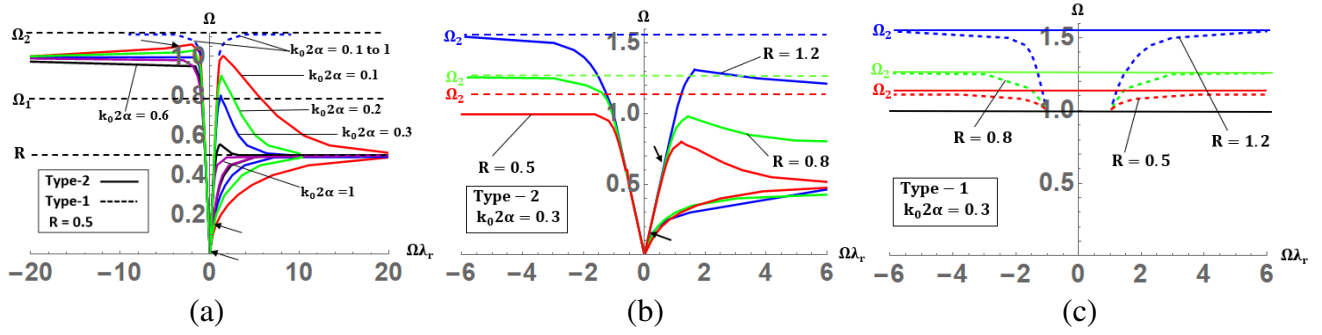
Figure 7. (a) Dispersion curves for (a) Type-1 and Type-2 surface waves for $R = 0.5$ in the range of $k_0 2\alpha = 0.1$ to 1, (b) Type-2 surface waves in the range of $R = 0.5$ to 1.2. (c) Type-1 surface waves in the range of $R = 0.5$–1.2.
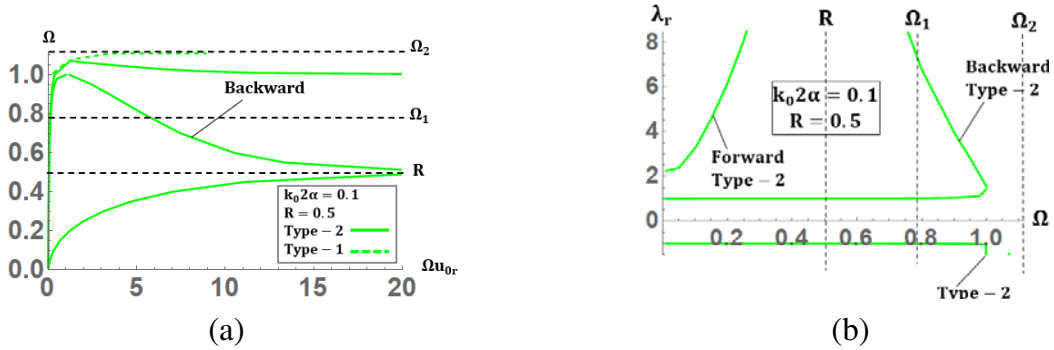
Figure 8. (a) Transverse wavenumber of the surface waves for $k_0 2\alpha = 0.1$. Continuous curves denote Type-2, whereas dashed curves Type-1 modes. (b) Surface modes' dispersion curves of β_z/k_0 versus normalized frequency Ω for a substrate thickness value $k_0 2\alpha = 0.1$ and $R = 0.5$.
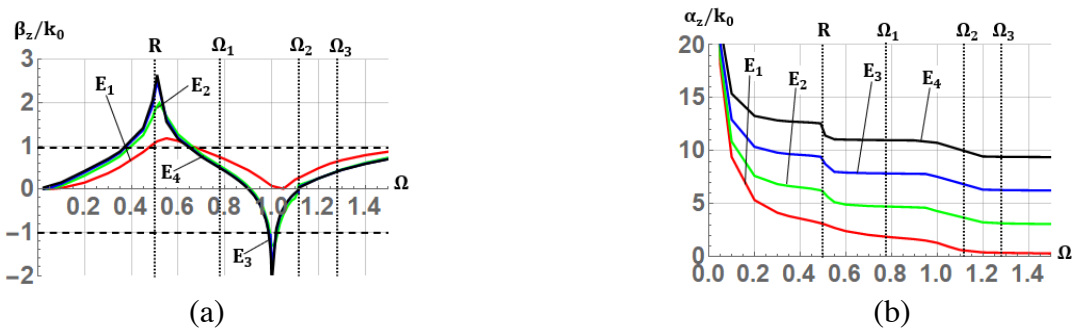
Figure 9. Dispersion curves of complex E modes of (a) phase and (b) attenuation constant vs frequency for $k_0 2\alpha = 1$ and $R = 0.5$ for complex modes in the range $\Omega = 0$ to 1.118. In the above figs. $\Omega_1 = 0.78$, $\Omega_2 = 1.118$ and $\Omega_3 = 1.28$.

of $G_{2+}(\lambda)$. Searching for these complex modes, we try to classify them according to criteria imposed by the literature [22, 24, 26, 27]. Complex modes can be distinguished from their $\mathrm{Re}(u_{0r})$ as proper $(\mathrm{Re}(u_{0r}) > 0)$ or improper $(\mathrm{Re}(u_{0r}) < 0)$. Each of them can be distinguished further, as fast $(\beta_z/k_0 < 1)$ or slow $(\beta_z/k_0 > 1)$ waves [22, 24]. The axial propagation constant (β_z/k_0) versus frequency for the first complex modes is shown in Fig. 9 for a thick substrate $k_0 2\alpha = 1$ and $R = 0.5$. It is observed that all of them exhibit possibly leaky wave bands $(\lambda_r < 1)$, as well as surface wave zones $(\lambda_r > 1)$. The next question is how these modes behave for different substrate thickness $k_0 2\alpha = 0.1$ to 1.2, and this
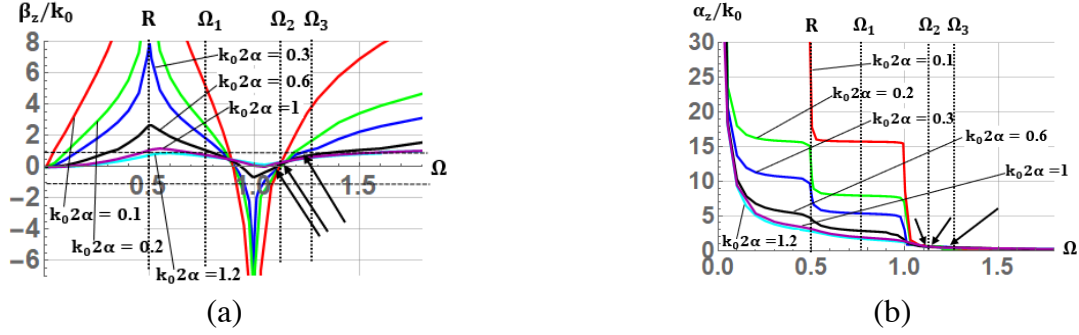
Figure 10. Dispersion curve ($R = 0.5$) of the first complex mode for various values of thickness $k_0 2\alpha$: (a) phase constant, (b) attenuation constant. Horizontal dashed lines indicate $\beta_z/k_0 = \pm1$. In the above figs. $\Omega_1 = 0.78$, $\Omega_2 = 1.118$ and $\Omega_3 = 1.28$.

is illustrated in Fig. 10 for the first leaky mode. In Fig. 10(a), the phase constant β_z/k_0 is examined versus the substrate thickness $k_0 2\alpha$ in order to reveal the thickness at which higher order improper surface and leaky waves are excited.

In order to classify these modes, their transverse propagation constant u_0 in the air region must be examined as in Fig. 10. Recall that the assumed dependence is $\propto e^{-k_0 u_0 x} = e^{-k_0 u_{0r} x} e^{-j k_0 u_{0i} x}$ for $u_0 = u_{0r} + j u_{0i}$. First, the radiation condition at infinity is fulfilled for $u_{0r} > 0$ which according to Fig. 10(a) is true for $\Omega > 0.9$ for $k_0 2\alpha = 0.6$, whereas for larger values of substrate thickness remains negative. Since the phase constant is positive ($u_{0i} > 0$ propagation toward $+\hat{x}$), as shown in Fig. 10(b), these are unexpected waves propagating both toward positive $\hat{z}$ and $\hat{x}$ or along the substrate and away from the structure. This is a unique feature of magnetized plasma and is due to positive but less than unity $0 \leq \epsilon_{r\,eff} \leq 1$ in the same band $\Omega_1 < \Omega < 1$. As $\mu_r = 1$ in this band, the index of refraction ($n_{eff} < 1$) is less than unity, and thus the excited waves are not bound to the plasma substrate, but instead they propagate (leak) away (toward $+\hat{x}$). This refractive phenomenon is expected to maximize "leakage" when the refractive index becomes unity ($n_{eff} = 1$, $\epsilon_{r\,eff} = 1$), as the substrate becomes transparent. Surface waves are expected to have a zero phase constant $u_{0i} = 0$ in the lossless case or to propagate inwards (toward $-\hat{x}$), as $u_{0i} < 0$ for $x > 0$ to feed plasma losses in the lossy case, e.g., Tamir & Oliner [4–6]. Thus Fig. 10 does not include any ordinary proper surface waves. On the other hand, leaky waves are expected to violate the radiation condition or $u_{0r} < 0$, but for ordinary substrates, ($\epsilon_{r\,eff} > 1$) the normalized phase constant in the axial direction should be less than unity or to behave as fast waves ($u_p > c_0$). Examining Figs. 10–11, it is observed that most of the range $0 < \Omega < \Omega_1$ supports leaky waves but for substrate thickness $k_0 2\alpha > 1.2$. For thinner substrates, there is a sub-band of slow waves ($\beta_z/k_0 > 1$), but these are propagating toward the positive transverse direction
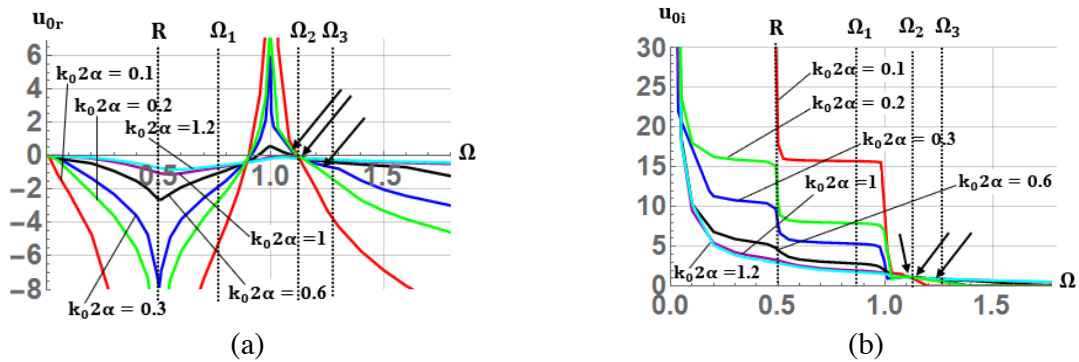
Figure 11. Depiction of transverse propagation constant u_0 of the first complex mode when $k_0 2\alpha = 0.1, 0.2, 0.3, 0.6, 1$ and 1.2: $(\alpha) u_{0r}$, (b) u_{0i}, versus normalized frequency Ω.

as $u_{0i} > 0$. Observing the results of Figs. 10–11 in the range $\Omega \leq 0.9$ and $\Omega > \Omega_2 = 1.118$ complex modes remain always improper, whereas in the range $0.9 \leq \Omega \leq \Omega_2$ these modes are transformed into proper complex. The presence of these modes, especially in magnetized plasma slabs has been noticed in [24, Part II, p. 180–181], and several discussions of their physical meaning have been presented by Oliner and Tamir in [6]. However, according to Figs. 10–11 they appear in frequency bands where ϵ_{r1} becomes negative ($\epsilon_{r1} < 0$), and they are excluded from the present research.

4.2. Field Expressions in the Spatial Domain

In the preceding sections, the field expressions are established in the spectral domain. In order to get usable results, these must be transformed to the spatial domain through the inverse Fourier transform of Eq. (2b). Since this inversion scheme involves a branch cut and different type pole singularities, these must be depicted in the complex z-plane in order to carry out the necessary integration. As explained before, the analysis will be restricted in the frequency range where ϵ_{r1} is positive ($\epsilon_{r1} > 0$) to ensure wave propagation in the exciting parallel plane waveguide, according to Eq. (12). Hence the range $R < \Omega < \Omega_2$ is excluded (Tables 4, 5) where surface waves become evanescent, and their contribution to radiation is negligible. One must also keep in mind that reversing the direction of the biasing static magnetic field from $+\hat{y}$ to $-\hat{y}$ causes ω_c and R to change sign (Eq. (3b)), and this reflects to a sign change in ϵ_{r2} according to Eq. (39) which is depicted in Fig. 5. Besides that, Seshadri [10] and Johansen [12] emphasize that the sign of ϵ_{reff} defines the behavior of surface waves. For lower frequencies surface modes and space wave govern total radiation [5], whereas for higher frequencies leaky wave contribution or space wave radiation is expected to dominate [28].

In view of the above task, the singularities for three indicative frequencies $\Omega = 0.01$, 0.15, and 1.24 are depicted in the complex $\lambda = 0$ plane (Fig. 12) for plasma with $R = \frac{\omega_c}{\omega_p} = 0.5$ (bias $-H_0\hat{y}$), which according to Eq. (60d) corresponds to $\Omega_1 = 0.781$, $\Omega_2 = 1.118$ and $\Omega_3 = 1.28$. A relatively thin substrate is considered $k_0 2\alpha = 0.3$ or $2\alpha = 0.0477\lambda_0$. Observing Fig. 10(a), for both cases $k_0 2\alpha = 0.3$ there is a low frequency leaky wave range $|\beta_z/k_0| < 1$ as well as a high frequency one between Ω_1 and Ω_3 ($\Omega_1 < \Omega < \Omega_3$). However, a closer look at their axial attenuation (α_z/k_0) constant Fig. 10(b) reveals that it is only beyond $k_0 2\alpha \geq 0.3$ that this attenuation α_z/k_0 becomes viable. Explicitly, Fig. 10(b) illustrates a cut-off phenomenon namely that the first leaky wave is turned on for $k_0 2\alpha \geq 0.3$. This is expected from regular dielectric substrates' experience, since at thicker substrates high order surface waves occur, which become leaky below their cut-off frequency. However, when a leaky mode does not exist its axial phase constant (β_z/k_0) should vanish, or the propagation constant tends to become purely real. The strange behavior here at the very low frequencies (β_z/k_0) still exists for $k_0 2\alpha < 0.3$ as

(a)   (b)
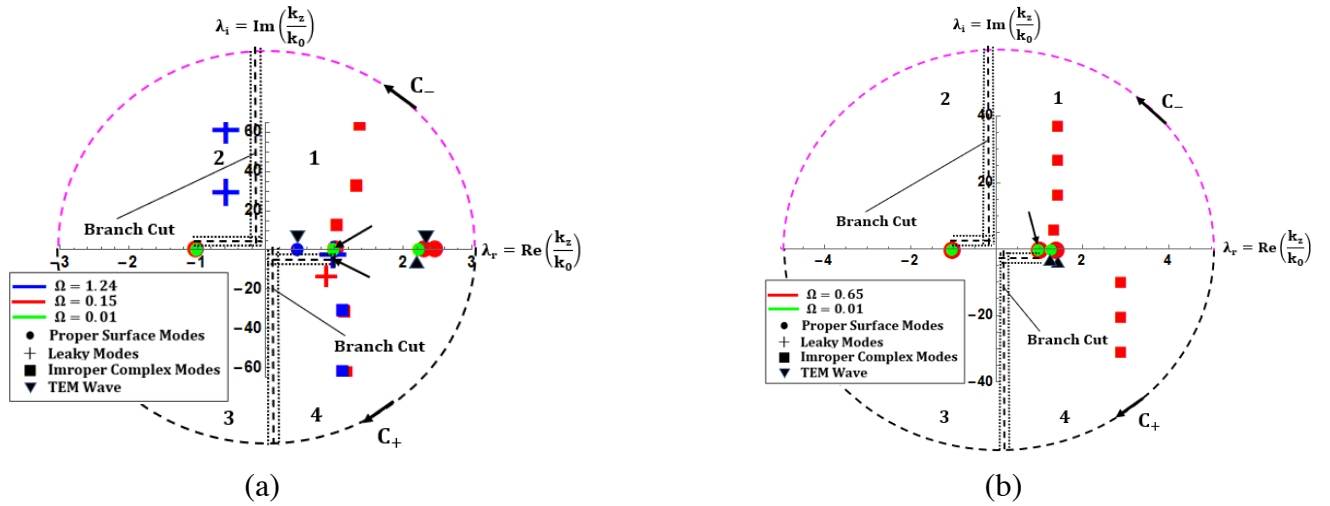
Figure 12. Integration contours in the complex λ-plane. Propagation constants are depicted for electrical thickness $k_0 2\alpha = 0.3$ when (a) $R = 0.5$ and (b) $R = 1.2$.

(a)   (b)
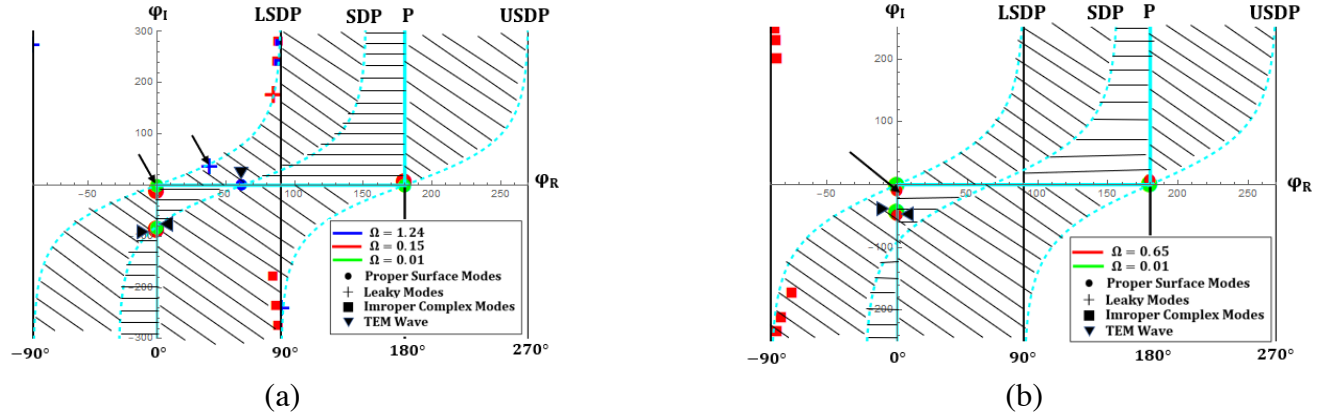
Figure 13. Pole locations on the steepest descent angle plane when $R = 0.5$ for electrical length $k_0 2\alpha = 0.3$ when (a) $R = 0.5$ and (b) $R = 1.2$. Extreme upper and lower steepest descent paths are indicated with dashed cyan lines, whereas original integration path with solid cyan line.

shown in Fig. 10(a). This unexpected behavior seems to be caused by the negative values of ϵ_{r2}, ϵ_{r3} and $\epsilon_{r\,eff}$ in this frequency range (Figs. 5–6), but the explicit analysis goes beyond the scope of this article. A second case is also considered for $k_0 2\alpha = 0.3$ for $R = 1.2$ in order to examine the frequency range $\Omega_1 < \Omega < R$ for $R > 1$. The integration contour depicted in Fig. 11 can be directly exploited for the calculation of the scattered (Equations (51)–(54)) near and far fields in the $z > 0$ region, while for the reflection coefficient and the field in the $z < 0$ region the contour must be closed in the upper λ-half plane as in Fig. 2. As noted, the pole contribution including the reflected TEM wave will be estimated from their residue contribution. For the near field, a numerical integration along the $\lambda_R = \text{Re}(\lambda)$ axis must be carried out, usually employing a Romberg quadrature scheme, but excluding poles which are encountered through their Cauchy principal value (half residue). The incident TEM wave is denoted as a dot marker plus a triangle marker on it, in Figs. 12–13.

The steepest descent approximation is employed for the far field calculation. For this purpose the usual sin() or cos() transformation from the complex $\lambda = \lambda_r + j\lambda_i$ plane to $\varphi = \varphi_r + j\varphi_i$ is performed wherein the branch-cut is removed as [19]: $\lambda = \lambda_r + j\lambda_i = \cos\varphi = \cos\varphi_r \cosh\varphi_i - j\sin\varphi_r \sinh\varphi_i$. The original integration path (P) along with the pole singularities of Fig. 12 cases is illustrated in Fig. 13. For the far field approximation, the integration path-P is deformed to its steepest descent counterpart, (SDP) which intersects the real axis at the saddle point $\varphi_r = \theta$, which is the observation angle. The SDP contour is closed by connecting it to the original path-P at infinity. From the radiation condition, the section at infinity has zero contribution, and the integration along P is equal to the integration along SDP plus the residue contributions from the poles enclosed between P and SDP (shaded area in Fig. 12). Notably, when a pole is close to either SDP or P but outside the shaded region, this must be "avoided" by drawing a small semicircle, but this still has a significant contribution to the integral equal to its Cauchy principal value (half residue). This contribution is accounted in [24, Part II], as well as by Ostner et al. [22]. What is of particular interest is to encounter the pole singularities that contribute to the integral when a radiation pattern is sought. For this purpose, the SDP paths for the two end-limiting observation angles $\theta = 0°$, $180°$ are drawn in Fig. 13 as LSDP and USDP, respectively. The cross-shaded region between them encounters all poles that will be captured. It is observed that both surface and leaky wave poles are encircled therein; however, improper complex wave poles ($\lambda_r > 1$) are outside this region [22].

4.3. Unidirectional Waves

It was as early as 1964 that Seshadri and Pickard [10] justified the existence of a special type of unidirectional surface waves. Their energy is found to concentrate either on the plasma-air or plasma-metal interfaces while they propagate toward the positive and negative $-\hat{z}$ directions (Fig. 1), respectively. Notably, these waves occur for low frequency ($\Omega \sim 0$) as the frequency increases or

with increased plasma thickness ($k_0\alpha \uparrow$), and unidirectional complex waves could be excited as well. A similar situation has already been examined in a recent work of Gangaraj and Monticone [29], who indeed encountered unidirectional leaky waves. Herein, both surface and complex unidirectional waves are observed and must be accounted in the near or far field evaluation. Unidirectional modes propagating toward $+\hat{z}$ have their energy concentrated in the air-plasma interface (upper surface), and they radiate significantly. On the opposite, unidirectional modes that propagate in the negative $-\hat{z}$ direction along the grounded surface are extremely rapidly attenuated inside the plasma, thus not affecting total radiated field [10].

4.3.1. Unidirectional Surface Waves

The reasoning for the grounded magnetized plasma to support unidirectional surface waves is already explained and justified in Section 4.1. The forward propagating unidirectional mode for $\Omega = 0.01$ and $R = 0.5$ thickness $k_0 2\alpha = 0.1$ and normalized axial propagation constant $\lambda = 1.00013$ is shown in the upper side (plasma air), interface in Fig. 13 with solid line blue curve. Changing the direction of the DC biasing magnetic field H_0 causes reversion of the gyromagnetic frequency, (ω_c). Unidirectional modes comprise poles of function $G_{2+}(\lambda)$. From insight in Fig. 3 and the works of [9, 10], only positive forward (poles λ_{pfs} of Fig. 3 with velocities $u_p \cdot u_g > 0$) and negative backward waves (poles λ_{nbs} of Fig. 3 with velocities $u_p \cdot u_g < 0$) contribute to the field. Thus, positive unidirectional modes propagate in the range $\Omega \to 0$ ($\lambda = 1.00013, \Omega = 0.01$), whereas unidirectional backward modes appear in the range $1 < \Omega < \Omega_2$ ($\lambda = -3.4, \Omega = 1.052$) (Fig. 7). As illustrated in Fig. 14, this reverse propagating modal energy is concentrated on the ground plane on the plasma surface $x = -\alpha$. In both cases, the energy concentration is denoted by the integral of Poynting Vector $\vec{P} = -\frac{1}{2}\text{Re}(E_x H_y^*) \cdot \hat{z}$ representing the propagating power density through the transverse cross-section [10]. These modes are also depicted by arrows on the dispersion curves of Figs. 7, 10, and 11.
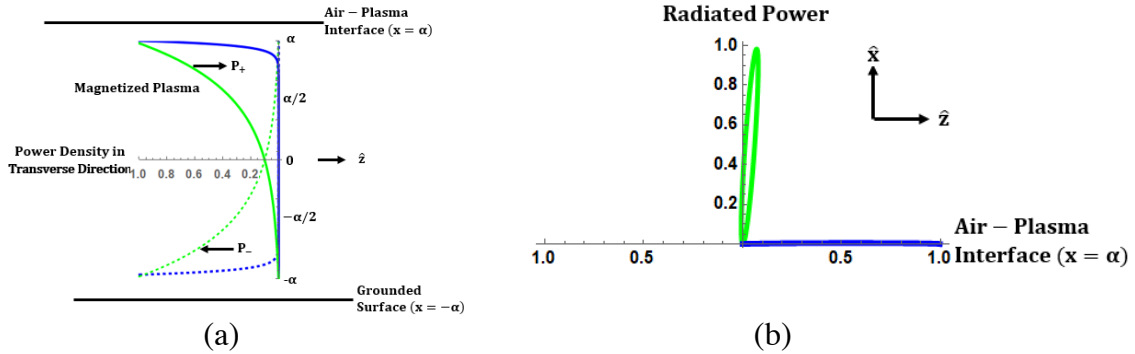
Figure 14. (a) Normalized, (to its maximum), power concentration over the transverse x-axis as a function of α, either on bottom, (dashed lines), or upper, (solid lines), surface for the proper surface, (blue curve), and leaky, (green curve), unidirectional modes. (b) Leaky mode radiation pattern is also presented in air region.

4.3.2. Unidirectional Complex Waves

As stated in [10], the unidirectional surface waves "become unidirectional leaky when the plasma thickness becomes finite". Notably, as explained in Section 4.1 only high order surface waves below their cut-off (turn-on) condition may become leaky with normalized axial propagation constant $\lambda < 1$. An example of unidirectional leaky waves for $\Omega = 1.1195$ is marked in the blue curve of Figs. 10–11, and its power density is illustrated in Fig. 13 with green line curve. The normalized propagation constant for the forward propagation (restricted around $x = +\alpha$) is $\lambda = 0.021 - j0.519$. Reverse propagating modes are those in #3 quadrant (Fig. 12) [10]. Obviously from Fig. 9, they propagate in the range $1 < \Omega < \Omega_2$. Notably, the forward propagating mode ($\lambda = 0.021 - j0.519, \Omega = 1.1195$) yields energy leakage in the air region as depicted in Fig. 14; however, the reverse ($\lambda = -0.055 - j0.548, \Omega = 1.112$) propagating

mode (dashed green line curve) cannot leak energy since it is bounded by the infinite ground plane. In the former case, the angle of maximum energy leakage-radiation is given by Jasik [30, Ch. 16, p. 16-7], as:

$$\theta = \cos^{-1}\left(\beta_z/\sqrt{\beta_z^2 + \beta_\rho^2}\right) = \cos^{-1}\left(\lambda_r/\sqrt{\lambda_r^2 + u_{0i}^2}\right) = \cos^{-1}\left(0.021/\sqrt{0.021^2 + 1.1265^2}\right) = 88.9° \quad (63)$$

The contributions of both surface and leaky waves poles to the near and far field evaluation are accounted for, through their residues.

4.4. Radiated Field

The far field generated by the structure of Fig. 1 is composed of the space or sky wave resulting from the integration around the branch cut (Figs. 3 or 12) and the propagating surface and leaky as well as complex surface waves' contributions accounted by their residues.

4.4.1. Space Wave Radiated Field

The space wave or the branch cut integral will be elaborated first for validation reasons, since this is also available by Seshadri & Pickard [10]. The power density of the radiated field is given by the Poynting vector $S(\theta)$ which for the plane wave in the far field is written as (where $\hat{\rho}$ is the radial unit vector in the xz-plane of Fig. 1 and θ is identical to φ as defined in [10]):

$$s(\theta) = \frac{1}{2}\text{Re}\left\{\hat{\rho} \cdot \vec{E}(\rho,\theta) \times \vec{H}^*(\rho,\theta)\right\} = \frac{1}{2}Z_0|H_y(\rho,\theta)|^2 = \frac{1}{2}Z_0\bar{S}(\theta) \quad (64)$$

The resulting normalized space wave power density $\bar{S}(\theta)$ is presented in Fig. 15 versus the angle θ defined from the $\hat{z}$-axis ($\theta = 0°$ enfire, $\theta = 90°$ broadside) for the case $R = 2.0$ and $\Omega = 1$ also considered in [8]. Although a magnetic line source oriented along the $\hat{y}$-axis is considered in [10], the normalized radiation patterns of Fig. 15 are found to be identical for different substrate thickness. For the verification presented in Fig. 15, both positive ($+$) and negative ($-$) G_2 functions are needed, in order to construct the G_2 function of Seshadri [10]. This can be explained by observing that the structure of Fig. 1 is also equivalent to a magnetic line source along-$\hat{y}$ with an equivalent magnetic current density $\vec{M}_{eq} = -(-\hat{z}) \times \hat{x}E_x^i = \hat{y}E_x^i$, where E_x^i is the electric field of the incident TEM-wave from Eq. (12).

In Fig. 16 the radiation pattern of $H_y(\theta)$ is plotted for four different values of gyromagnetic frequency R. Recall that $H_y(\theta)$ is defined in Eq. (52) and finally in Eq. (59) as a product of the even function and non-even function. It is observed from Figs. 16(a)–(b) that the even term remains independent from changes of gyromagnetic frequency R, and only the non-even term varies. H_y field receives its peak value at the lowest value of frequency R, e.g., $R = 0.5$. In Fig. 17 the radiation pattern $H_y(\theta)$ is plotted for four different values of the substrate's thickness $k_02\alpha$ versus the observation angle. Separate representations are given for the even Kernel function in Fig. 17(a), the non-even Kernel function in Fig. 17(b), and as a product of the two of them in Fig. 17(c). In the radiation pattern of
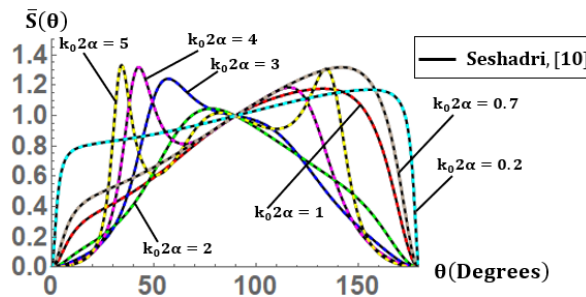
Figure 15. Space wave radiated energy flow $\bar{S}(\theta)$ with respect to observation angle assuming $R = 2$ and $\Omega = 1$, compared against Seshadri [10].
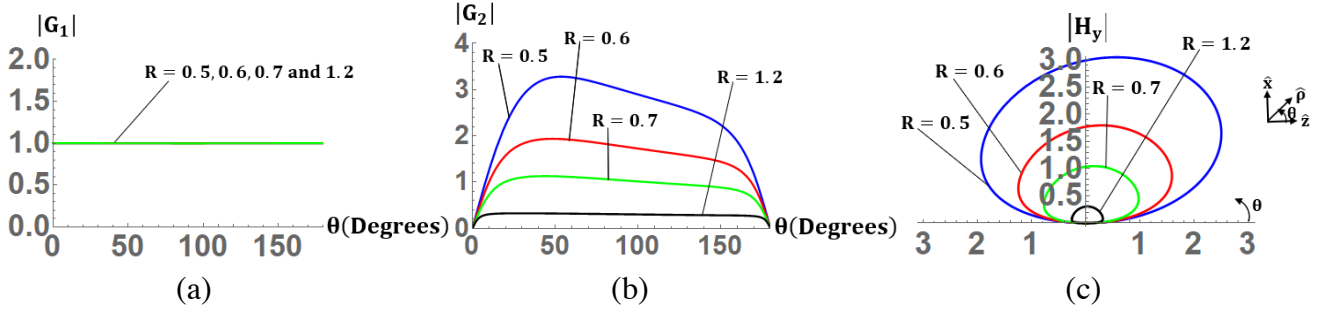
Figure 16. Space wave radiation pattern of $|H_y|$ field's space wave as a product of the Kernel functions: (a) even Kernel function, (b) non-even Kernel function and (c) product of two functions in polar coordinates for four different values of gyromagnetic frequency at frequency $\Omega = 1$, considering plasma thickness $k_0 2\alpha = 0.1$.
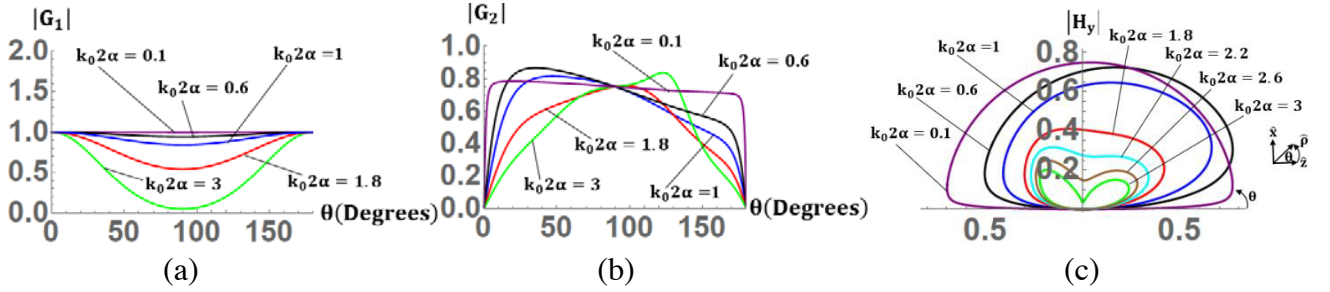
Figure 17. Space wave radiation pattern of $|H_y|$ field's space wave as a product of the Kernel functions (a) even Kernel function, (b) non-even Kernel function and (c) product of two functions in polar coordinates for six different values of plasma slab thickness at frequency $\Omega = 1$, considering gyromagnetic frequency $R = 2$.

non-even Kernel, which includes plasma anisotropy in Fig. 17(b), there is always a broad maximum near the broadside direction, a null in the end-fire direction, and in between, sharply defined peaks whose number increases with the thickness $k_0 2\alpha$. Fig. 17 reveals that for small substrate thickness the even part G_1 is almost uniform across θ, and the observed maxima in the radiation are due to the non-even part G_2. As the substrate thickness increases the even part G_1 starts to form lobes but presenting a maximum at end-fire. However, this disappears in the total field, due to the corresponding nulls of G_2.

4.4.2. Total Radiated Field — Poles Contribution

Leaky modes, with significant contribution in total radiation, are those with $\beta_z > \alpha_z$ [22, 24, 28, 31]. Indeed, they contribute in a two-maxima split beam [31], because of the symmetry of their solutions ($\pm k_{pz}$). However, in the present problem the anisotropic electric permittivity tensor results in a lack of poles' symmetry (Fig. 12). As illustrated in Figs. 12–13, surface and leaky wave poles are captured by the integration path, besides the space wave (branch cut integral). Among the tested thickness of Figs. 10–11, $k_0 2\alpha = 0.3$ is chosen, as it is the only one where leaky modes with viable losses appear. $|H_y|$ component is depicted initially performing saddle point method on the integrand $G_{1+}G_{2+}$ (blue curve). Next, residues are evaluated from Eq. (52) (red or green curve in Fig. 18). Finally, total field is evaluated by adding to the residue contribution the full form of space wave in Eq. (59). Modal contribution is evaluated through Three frequencies are chosen: #1) $\Omega = 0.15$, $R = 0.5 < 1$, #2) $\Omega = 0.65$, $R = 1.2 > 1$ and #3) $\Omega = 1.24$, $R = 0.5 < 1$ that cover all the examined range of Tables 4–5. The radiation pattern in the first case is presented in the Fig. 18(a) where one may observe that this is dominated by space wave, while in the second case (Fig. 18(b)), surface wave dominates. On the contrary for the high frequency case at $\Omega = 1.24$, the surface wave disappears; the space wave beam
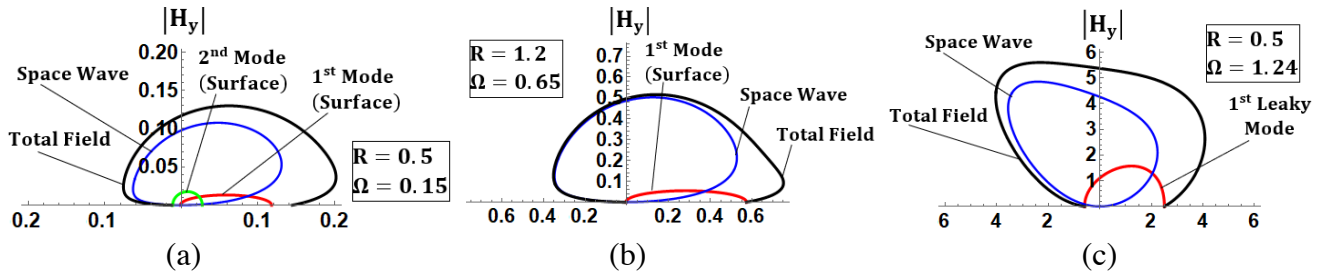
Figure 18. Normalized total radiated far field $|H_y|$ for slab's electrical length thickness $k_0 2\alpha = 0.3$ including space wave and the modal contribution: (a) $\Omega = 0.15$, $R = 0.5$, (b) $\Omega = 0.65$, $R = 1.2$, (c) $\Omega = 1.24$, $R = 0.5$.

becomes stronger; and the first leaky wave with a pole $\lambda = 0.985 - j0.486$ is captured with a significant contribution as shown with red curve in Fig. 18(c).

4.4.3. Near Field

In order to get a view in the near field, the integration along the original path depicted in Fig. 13 must be carried out. Instead of performing a numerical integration along the real axis, the closed path $C_\pm$ is again considered resulting in branch cut integral and the residue contribution of the enclosed poles. However, in this case the branch cut integral (space wave) cannot be approximated by the steepest descent, and it must be performed numerically. Indeed, Mathematica [21] is utilized for this purpose, and the two cases $k_0 2\alpha = 0.3$ studied in Fig. 18 are considered again but for a small distance $k_0\rho = 0.05$ and 1.5. So, the $G_{1+}G_{2+}$ terms of Eq. (56) are evaluated through performing numerical integration. A third larger distance $k_0\rho = 1.5$ is also considered. These results are illustrated in Fig. 19. In the low frequency case $\Omega = 0.65$ shown in Fig. 19(a), the total field is similar to the radiated one with dominance of the surface wave, but the small space wave is now almost isotropic. Likewise, in the high frequency $\Omega = 1.24$ case Fig. 19(b) the only difference is the isotropic form of the space wave. In the near field, the intensity is mainly governed by the poles' contribution. This is in accordance to Tamir and Oliner [27, Sec. 3], who noticed that the intensity in near field is mainly owed to the presence of leaky or surface wave poles, not to space wave. Observing the field at a larger distance $k_0\rho = 0.5$ the space wave starts to become directional as in the far field situation. Finally, at distance $k_0\rho = 1.5$ the produced field exhibits the far field behavior, as it is concluded from a direct comparison between Figs. 18–19.

Since it is considered necessary both by Fikioris et al. [16] and by Bates and Mittra [44], the field component E_z should be evaluated both in the far field and in near field, in order for the boundary value conditions to be verified. Thus, the total radiated far field E_z is plotted in cartesian axes following Eqs. (8), (37), and (59) as depicted in Fig. 20. The near field axial component E_z is also plotted at
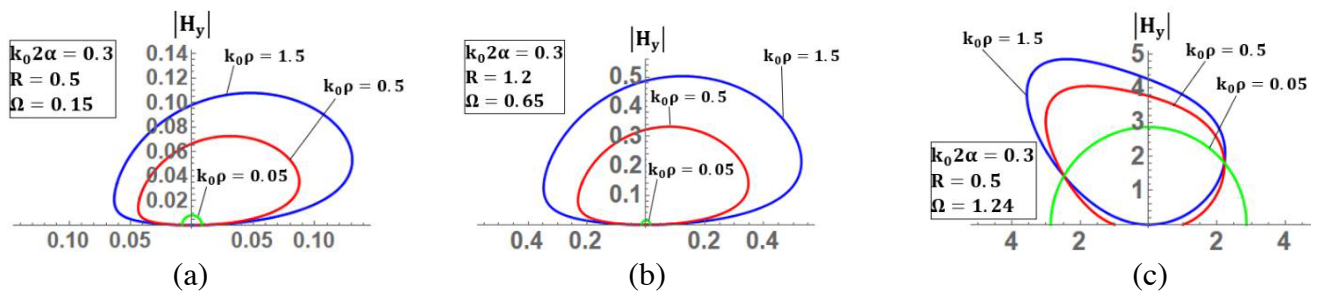
Figure 19. Near field for electrical length $k_0 2\alpha = 0.3$ and distance $k_0\rho = 0.05$ to 1.5, including space wave contribution: (a) $\Omega = 0.15$ and $R = 0.5$, (b) $\Omega = 0.65$ and $R = 1.2$, (c) $\Omega = 1.24$ and $R = 0.5$, when leaky wave is excited.
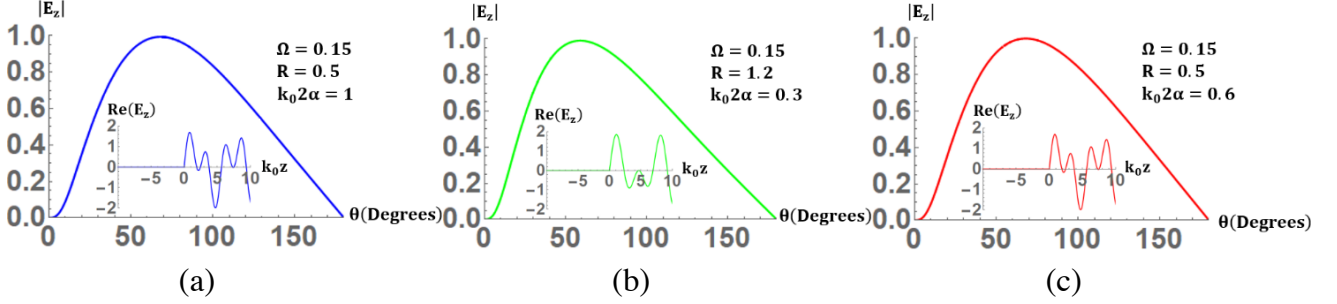
Figure 20. Total axial electric field E_z: Space wave far field with corresponding near field as inset at $\Omega = 0.15$: (a) $k_0 2\alpha = 1$ and $R = 0.5$, (b) $k_0 2\alpha = 0.3$ and $R = 1.2$, (c) $k_0 2\alpha = 0.6$ and $R = 0.5$.

the interface $x = \alpha$ and over the truncated upper conductor to ensure the related boundary condition. Indeed, the real part of near field E_z (inset) is zero for $z < 0$ (upper plane of parallel plane waveguide at $x = \alpha$), and non-zero for $z > 0$ (air-plasma interface $x = \alpha$), verifying the boundary conditions for the tangential electric field components. Also, the far field component E_z vanishes at the endfire ($\theta = 0°$ or $180°$) direction expressing a similar behavior to the respective electric field component in the similar structures of [16] or [44]. Thus, the essential boundary conditions are satisfied, acting as a verification to the methodology elaborated herein.

4.4.4. TEM Wave Reflection Coefficient

We recall at this point that the incident TEM wave yields a scattering field including higher order modes around the aperture at $z = 0$. However, at a distance of about a quarter TEM wavelength away from the edge toward the parallel waveguide region ($z < 0$ in Fig. 1), all these higher order modes vanish, and only the reflected TEM wave exists. The related reflection coefficient is defined in Eq. (50). This is evaluated for a gyromagnetic frequency corresponding to $R = 0.5$ and three different substrate thicknesses $k_0 2\alpha = 0.15$, 0.2, and 0.3, and the results are presented in Fig. 21(a).

A very strange situation is observed at three frequencies $\Omega = 0, R, \Omega_2$ where the reflected field vanishes. Observing Figs. 5–6, this condition corresponds to infinite $\epsilon_{r1} \to \infty$, $\epsilon_{r2} \to -\infty$, $\epsilon_{r3} \to -\infty$ at $\Omega = R$ and infinite ϵ_{reff} at $\Omega = 0, \Omega_2$. On the contrary, a total reflection occurs in the band $\Omega = R$ to Ω_2. From Figs. 5–6, it is again observed that this virtual short circuit situation corresponds to $\epsilon_{r1} < 0$ and $\epsilon_{r2} > 0$. These phenomena are of particular interest in practical applications and require further exploration. Also, the phase of the reflection coefficient is depicted in Fig. 21(c) where it is observed that it becomes zero throughout the frequency range of Ω from R up to Ω_2. Explicitly, this range corresponds to the frequency region where ϵ_{r1} becomes negative (Fig. 4(a), Table 5), or the incident TEM wave in Eq. (50a) becomes evanescent. This means that both incident and reflected waves are exponentially damped [12]. Thus, reflection coefficient exhibits null argument, becoming purely real [32, p. 169], and the ratio of these damped waves' amplitudes at the edge ($z = 0$, $x = \alpha$) is depicted in Fig. 21(a) for the
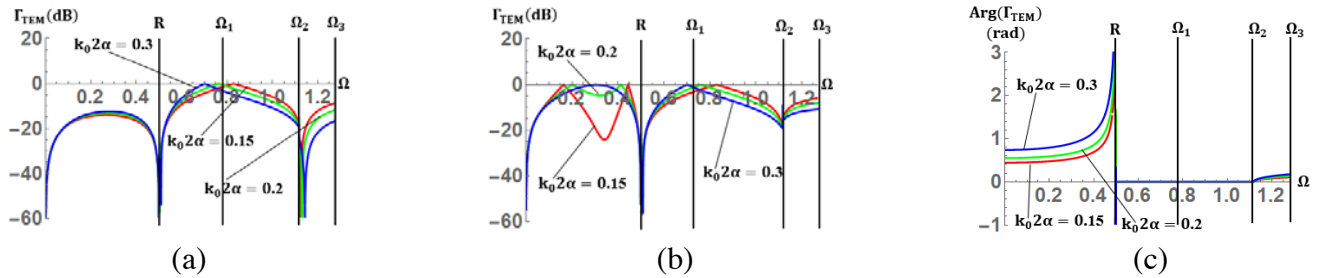
Figure 21. Reflection coefficient of the incident TEM wave vs normalized frequency Ω: (a) $R = 0.5$, (b) $R = -0.5$ and (c) argument ($R = 0.5$).

range $R < \Omega < \Omega_2$. Notably, the phase of the TEM radiation coefficient is an important quantity as it can be exploited in patch antennas printed on magnetized plasma substrate in order to estimate their resonance conditions, e.g., [33]. The reflection coefficient when the dc bias is reversed is illustrated in Fig. 21(b). Similar phenomena are observed in this case, which are in accordance with the dielectric constant behavior in Fig. 5 and Table 4. Reverse bias causes opposite sign to ϵ_{r2} (Fig. 5(b)), but it retains the same sign in ϵ_{r1}. Thus, differences between Figs. 21(a) and (b) are expected, since the reflection coefficient is not an even function.

5. CONCLUSIONS AND DISCUSSION

An extended Wiener-Hopf technique has been employed to analyze and evaluate the guiding and radiating properties of an anisotropic plasma-loaded, parallel plate waveguide with a truncated upper plate. The anisotropy of the plasma arises from a biasing constant magnetic field parallel to the edge of the truncated upper plate. The analysis is restricted to the normal incidence of the extra-ordinary TEM wave propagating in the parallel plane region, and thus only TM type waves are excited. Due to the non-reciprocal nature of the structure, the kernel of the Wiener-Hopf equation is non-symmetrical, and its factorization is not established. There is only one similar publication by Fikioris et al. [16], elaborating on magnetized ferrites. Herein, their approach is extended to the magnetized plasma case. Important nonreciprocal and unidirectional phenomena are involved as a result of the magnetized plasma anisotropy. The main goal of factorizing the Wiener-Hopf kernels for the open geometry problem is achieved herein. The far field as well as the near field of the structure is extensively studied, including the contribution of proper surface, improper leaky modes, and complex surface wave as well as the unique unidirectional waves. Significant changes of the operational characteristics of the structure can be achieved by varying the intensity of the biasing magnetic field. This fact implies certain important practical application of the guiding or radiating structure.

Both the theory and numerical results are validated against the few available publications. In the factorization, a detailed comparison of the present effort with the work of Fikioris et al. [16] on tunable ferrite structures was presented. There the various similarities and differences were enlisted and taken into consideration. The new terms were fully justified, treated accordingly, and their meaning and consequences were addressed. It was also verified that in any case the factorized kernel and the unfactorized one give identical values. In the numerical implementation Eq. (53) was checked to comply with the near field boundary condition of zero tangential electric field on the upper truncated metal conductor. Furthermore, the present results were successfully compared with available published results from the open literature [10]. The validations against Seshadri and Pickard [10] works have confirmed the present theory for both the excited modes as well as for the sky-space wave radiation. As a further check, it was verified that the near field results obtained through numerical integration match the far field results estimated by steepest descent, as the distance from the structure is increased. The space as well as the total radiation pattern was also qualitatively compared against Johansen's [12] results. The qualitative feature results from the fact that although the Johansen's structure seems similar it assumes uniform plasma space beyond the truncated edge.

REFERENCES

1. Hoyaux, M. and P. Gans, "Theorie des oscillations spontanees dans les tubes a vapeur de mercure a cathode chaude," *Defense Technical Information Center*, 1956.

2. Chabries, D. M. and D. M. Bolle, "Impulse reflection with arbitrary angle of incidence and polarization from isotropic plasma slab," *Radio Science*, Vol. 6, No. 12, 1143–1149, 1971.

3. Bolle, D. M., "Utilization of surface magnetoplasmons in the millimetre wavelength range," *IEEE Proc. on Microwaves, Antennas and Propagation*, Vol. 140, No. 3, 174–182, 1993.

4. Oliner, A. A. and T. Tamir, "Backward waves on isotropic slab," *J. Appl. Physics*, Vol. 33, 231–233, 1962.

5. Tamir, T. and A. A. Oliner, "The influence of complex waves on the radiation field of a slot-excited plasma layer," *IEEE Trans. on Antennas and Propagation*, Vol. 10, No. 1, 55–64, Jan. 1962.

6. Tamir, T. and A. A. Oliner, "The spectrum of electromagnetic waves guided by a plasma layer," *IEEE Proc.*, Vol. 51, 317–331, Feb. 1963.

7. Angulo, C. and W. Chang, "The launching of surface waves by a parallel plate waveguide," *IRE Trans. Antennas and Propagation*, Vol. 7, No. 4, 359–368, Oct. 1959.

8. Bates, C. P. and R. Mittra, "Waveguide excitation of dielectric and plasma slabs," *Radio Science*, Vol. 3, No. 3, 251–266, Mar. 1968.

9. Kyriacou, G. A., "Wiener-Hopf analysis of planar canonical structures loaded with longitudinally magnetized plasma biased normally to the extraordinary wave propagation," *Progress In Electromagnetics Research B*, Vol. 5, 1–34, 2008.

10. Seshadri, S. R. and W. F. Pickard, "Surface waves on an anisotropic plasma sheath," *IEEE Trans. on Microwave Theory and Techniques*, Vol. 12, No. 5, 529–541, 1964.

11. Pathak, P. H. and R. G. Kouyoumjian, "TM surface wave diffraction by a truncated dielectric slab recessed in a perfectly conducting surface," *NASA Contractor Report*, May 1974.

12. Johansen, E. L., "The radiation properties of a parallel-plane waveguide in a transversely magnetized, homogeneous plasma," *IEEE Trans. on Microwave Theory and Techniques*, Vol. 13, No. 1, 77–83, 1965.

13. Mitsalas, X. M., A. V. Kudrin, and G. A. Kyriacou, "Analytical study of surface and leaky waves on a grounded magnetized plasma slab," *PIERS Proceedings*, 1526–1532, Moscow, Russia, Aug. 19–23, 2012.

14. Mittra, R. and S. W. Lee, *Analytical Techniques in the Theory of Guided Waves*, The MacMillan Company, New York, 1971.

15. Bates, C. P. and R. Mittra, "A factorization procedure for Wiener-Hopf kernels," *IEEE Trans. on Antennas and Propagation*, Vol. 17, No. 1, 102–103, Jan. 1969.

16. Fikioris, J. G., J. L. Tsalamengas, and N. K. Uzunoglu, "Analysis of a semi-infinite microstrip patch loaded with a ferrite substrate," *Electromagnetics*, Vol. 3, 271–288, 1983.

17. Noble, B., *Methods Based on the Wiener-Hopf Technique*, Pergamon Press, 1958.

18. Daniele, V. G., "An introduction to the Wiener-Hopf technique for the solution of electromagnetic problems," *Lecture Notes*, 2007.

19. Felsen, L. B. and N. Marcuvitz, *Radiation and Scattering of Waves*, IEEE Series on Electromagnetic Wave Theory, Wiley-IEEE Press, 1994.

20. Abramowitz, M. and I. A. Stegun, *Handbook of Mathematical Functions with Formulas, Graphs and Mathematical Tables*, Dover Books on Mathematics, 1965.

21. Software of WOLFRAM MATHEMATICA 11.1.

22. Ostner, H., J. Detlefsen, and D. R. Jackson, "Radiation from one-dimensional leaky-wave antennas," *IEEE Trans. on Antennas and Propagation*, Vol. 43, No. 4, 331–339, Apr. 1995.

23. Mesa, F., C. D. Nallo, and D. R. Jackson, "The theory of surface-wave and space-wave leaky mode excitation on microstrip lines," *IEEE Trans. on Microwave Theory and Techniques*, Vol. 47, No. 2, 207–215, Feb. 1999.

24. Collin, R. E. and F. Zucker, *Antenna Theory. Part I & II*, McGraw Hill, 1969.

25. Pozar, D. M., *Microwave Engineering*, 3rd edition, J. Wiley, 2007.

26. Tamir, T. and A. A. Oliner, "Guided complex waves. Part I: Fields at an interface," *Proc. IEE*, Vol. 110, 310–324, Feb. 1963.

27. Tamir, T. and A. A. Oliner, "Guided complex waves. Part II: Relation to radiation patterns," *Proc. IEE*, Vol. 110, 325–334, Feb. 1963.

28. Kim, K. Y., "Guided and leaky modes for circular open electromagnetic waveguides: Dielectric, plasma and metamaterial column," Ph.D. Thesis, Dec. 2004.

29. Gangaraj, S. A. H. and F. Monticone, "Topologically-protected one-way leaky waves in nonreciprocal plasmonic structures," *Journal of Physics Condensed Matter*, Vol. 30, No. 10, Feb. 2018.

30. Jasik, H., *Antenna Engineering Handbook*, 1st edition, McGraw Hill, 1961.

31. Lovat, G., P. Bughignoli, and D. R. Jackson, "Fundamental properties and optimization of broadside radiation from uniform leaky-wave antennas," *IEEE Trans. on Antennas and Propagation*, Vol. 54, No. 5, 1442–1452, May 2006.

32. Barkeshli, K., *Advanced Electromagnetics and Scattering Theory*, 1st edition, Springer, 2015.

33. Kyriacou, G. A. and J. N. Sahalos, "The edge admittance model for the study of microstrips on uniaxial substrate," *Archiv fur Elektrotechnik*, Vol. 76, 169–179, 1993.

34. Kuester, E. F., R. T. Johnk, and D. C. Chang, "The thin-substrate approximation for reflection from the end of a slab-loaded parallel-plate waveguide with application to microstrip patch antennas," *IEEE Trans. on Antennas and Propagation*, Vol. 30, No. 5, 910–917, 1982.

35. El-Sherbiny, A. M., "Exact analysis of shielded microstrip lines and bilateral fin lines," *IEEE Trans. on Microwave Theory and Techniques*, Vol. 29, No. 7, 669–675, 1981.

36. Kyriacou, G. A., *Wiener Hopf Type Analysis of Microstrip Structures*, Vol. 171, Springer, 2000.

37. Talisa, S. H. and D. M. Bolle, "Performance predictions for isolators and differential phase shifters for the near millimeter wave range," *IEEE Trans. on Microwave Theory and Techniques*, Vol. 29, No. 12, 1338–1343, 1981.

38. Iqbal, S. S. and A. A. Gibson, "Characteristics of millimeter-wave semiconductor phase shifters," *International Conf. on Ant. and Prop.*, 323–326, Apr. 2001.

39. Taya, S. A. and T. M. El-Agez, "A reverse symmetry optical waveguide sensor using a plasma substrate," *Journal of Optics*, Vol. 13, No. 7, 075701, 2011.

40. Taya, S. A., "Slab waveguide with air core layer and anisotropic left handed material claddings as a sensor," *Optoelectronics Review*, Vol. 22, No. 4, 252–257, 2014.

41. Taya, S. A., "Theoretical investigation of slab waveguide sensor using anisotropic metamaterial," *Optica Applicata*, Vol. XLV, No. 3, 405–417, 2015.

42. Taya, S. A., "Dispersion properties of lossy dispersive and anisotropic left handed material slab," *Optik*, Vol. 126, No. 14, 1319–1323, 2015.

43. Huang, T., G. B. Liu, H. F. Zhang, and L. Zeng, "A new adjustable frequency waveguide circularly polarized antenna based on the solid state plasma," *Applied Physics A*, Vol. 125, No. 660, 2019.

44. Bates, C. P. and R. Mittra, "A technique for solving certain Wiener-Hopf type boundary value problems," *Antenna Laboratory Report*, No. 66-4, 1966.